TIMP1 mediates astrocyte-dependent local immunosuppression in brain metastasis acting on infiltrating CD8+ T cells

TIMP1 mediates astrocyte-dependent local immunosuppression in brain metastasis acting on infiltrating CD8+ T cells.

*Running title: Astrocyte-dependent immunosuppression in brain metastasis.

Neibla Priego[1*], Ana de Pablos-Aragoneses[1], María Perea-García[1], Valentina Pieri[1+], Carolina Hernández-Oliver[1], Laura Álvaro-Espinosa[1], Andrea Rojas[1@], Oliva Sánchez[1], Ariane Steindl[1$], Eduardo Caleiras[2], Fernando García[3], Santiago García-Martín[4], Osvaldo Graña-Castro[4#], Sandra García-Mulero[5,6], Diego Serrano[7], Paloma Velasco-Beltrán[8,] Borja Jiménez-Lasheras[8], Leire Egia-Mendikute[8], Luise Rupp[9], Antonia Stammberger[9], Matthias Meinhardt[10], Anas Chaachou-Charradi[11], Elena Martínez-Saez[11], Luca Bertero[12,13], Paola Cassoni[12,13], Luca Mangherini[12,13], Alessia Pellerino[14], Roberta Rudà[14], Riccardo Soffietti[15], Fatima Al-Shahrour[4], Paul Saftig[16], Rebeca Sanz-Pamplona[5,17,18], Marc Schmitz[9,19,20], Stephen J Crocker[21], Alfonso Calvo[7], Asís Palazón[8,22], RENACER[23], Manuel Valiente[1*].

1 Brain Metastasis Group, Spanish National Cancer Research Centre (CNIO), Madrid, Spain.
2 Histopathology Unit, Spanish National Cancer Research Centre (CNIO), Madrid, Spain.
3 Proteomics Unit, Spanish National Cancer Research Centre (CNIO), Madrid, Spain.
4 Bioinformatics Unit, Spanish National Cancer Research Centre (CNIO), Madrid, Spain.
5 Biomarkers and Susceptibility Unit, Oncology Data Analytics Program (ODAP), Catalan Institute of Oncology (ICO), Bellvitge Biomedical Research Institute (IDIBELL), L'Hospitalet de Llobregat, Spain.
6 Department of Pathology and Experimental Therapy, School of Medicine, University of Barcelona (UB), L'Hospitalet de Llobregat, Barcelona, Spain.
7 Center for Applied Clinical Research (CIMA); Department of Pathology, Anatomy and Physiology, Faculty of Medicine, University of Navarra; IdISNA, Pamplona, Spain; CIBERONC, Madrid, Spain.
8 Cancer Immunology and Immunotherapy Lab, Center for Cooperative Research in Biosciences (CIC BioGUNE), Basque Research and Technology Alliance (BRTA), Derio, Spain.
9 Institute of Immunology, Faculty of Medicine Carl Gustav Carus, TU Dresden, Dresden, Germany.
10 Department of Pathology, Faculty of Medicine Carl Gustav Carus, TU Dresden, Dresden, Germany.
11 Pathology Department, Vall d'Hebron Hospital, Barcelona, Spain.
12 Department of Medical Sciences, University of Turin, Turin, Italy.
13 Pathology Unit, Department of Laboratory Medicine, Città della Salute e della Scienza University Hospital, Turin, Italy.
14 Division of Neuro-Oncology, Department of Neuroscience " Rita Levi Montalcini", University and City of Health and Science Hospital, Turin, Italy.
15 Candiolo Cancer Institute, FPO-IRCCS, Candiolo, Turin, Italy.
16 Biochemical Institute, Christian-Albrechts-Universität Kiel, Kiel, Germany.
17 University Hospital Lozano Blesa, Aragon Health Research Institute (IISA), ARAID Foundation, Aragon Government, Zaragoza, Spain.

18 Centro de Investigación Biomédica en Red de Epidemiologia y Salud Pública (CIBERESP), Spain.
19 National Center for Tumor Diseases (NCT) Dresden, Dresden, Germany.
20 German Cancer Consortium (DKTK), partner site Dresden, and German Cancer Research Center (DKFZ), Heidelberg, Germany.
21 Department of Neuroscience, University of Connecticut School of Medicine, Farmington, USA.
22 Ikerbasque, Basque Foundation for Science, Bizkaia, Spain.
23 Biobank, Spanish National Cancer Research Centre (CNIO), Madrid, Spain.

#Current address: Instituto de Medicina Molecular Aplicada (IMMA) Nemesio Díez, Basic Medical Science Department, Medicine School, Universidad San Pablo-CEU, CEU Universities, Boadilla del Monte. Spain.
+Current address: Vita-Salute San Raffaele University, Milan, Italy.
@ Current address: School of Medicine, University Autónoma, Madrid, Spain.
$Current address: Division of Oncology, Department of Medicine I, Medical University of Vienna, Vienna, Austria.
*Corresponding author

Corresponding author information:

Manuel Valiente
Spanish National Cancer Research Centre (CNIO), C/ Melchor Fernández Almagro, 3, 28029, Madrid, Spain.
mvaliente@cnio.es
+34 917 328 000 ext. 3035

Neibla Priego
Spanish National Cancer Research Centre (CNIO), C/ Melchor Fernández Almagro, 3, 28029, Madrid, Spain.
npriego@cnio.es
+34 917 328 000 ext. 3031

Declaration of interests

The authors declare no conflict of interest

Abstract

Immunotherapies against brain metastases have shown clinical benefits when applied to asymptomatic patients, but they are largely ineffective in symptomatic cases for unknown reasons. Here we dissect the heterogeneity in metastasis-associated astrocytes using scRNAseq and report a population that blocks the antitumoral activity of infiltrating T cells. This pro-tumoral activity is mediated by the secretion of TIMP1 from a cluster of pSTAT3^{+} astrocytes that acts on CD63^{+} CD8^{+} T cells to modulate their function. Using genetic and pharmacologic approaches in mouse and human brain metastasis models, we demonstrate that combining immune checkpoint blockade antibodies with the inhibition of astrocyte-mediated local immunosuppression may benefit patients with symptomatic brain metastases. We further reveal that the presence of TIMP1 in liquid biopsies provides a biomarker to select patients for this combined immunotherapy. Overall, our findings demonstrate an unexpected immunomodulatory role for astrocytes in brain metastases with clinical implications.

State of significance

This study presents a significant advance in the understanding of immunomodulation in brain tumors and offers new insights into the potential therapeutic interventions for brain metastases.

Introduction

The general dismal diagnosis of brain metastasis is starting to evolve into a more complex situation where significant differences in prognosis exist depending on the state of the disease (i.e., local only versus local and systemic) (1), or the presence of vulnerabilities for which specific targeted drugs have demonstrated substantial benefits (1). Similarly, immunotherapies based on immune checkpoint blockade (ICB) have been proved equally effective both on intracranial and on extracranial metastases in several clinical trials including melanoma and lung cancer patients (2–8). Although variability of the responses is broad and not all patients benefit from it, the use of ICB to treat brain metastasis is widespread. However, many questions remain such as whether or not the therapeutic antibodies do get access to the brain or instead play their role extracranially and then activated T cells infiltrate the CNS (1,9–11). Even more interesting is that, almost all clinical trials have been developed on asymptomatic brain metastases. Thus, the symptomatic state, which is the clinically relevant one, remains poorly studied in the context of immunotherapy. Interestingly, in the limited reports where ICB has been tested on symptomatic brain metastases the therapeutic response rate dropped dramatically (2,7). Although the reason behind the differential response of brain metastases to ICB is unknown, several reasons have been put forward. One of the main explanations is the use of corticoids in symptomatic brain metastasis as the cornerstone strategy to control edema. As a potent immunosuppressor corticoids have been suggested to impair the effect of ICB, however available preclinical data and metanalysis of clinical trials cannot assign the full responsibility to this drug (12–14).

The colonization of the brain by metastatic cells involves changes in the microenvironment. Initially, metastatic cells face a reactive glial response eliminating many of the cancer cells that completed extravasation (15). Subsequently, as the surviving cancer cells resume their growth, they start modifying the environment. As such, altered molecular patterns emerge *de novo* in specific cellular components of the brain. STAT3 is activated in a subpopulation of reactive astrocytes only in advanced stages of the disease when the metastasis has reached a certain size (16). This disease-associated altered molecular pattern contributes significantly to maintain the viability of the metastasis by protecting cancer cells (16). Remarkably, this dependency on a component of the microenvironment was translated into a novel therapeutic opportunity validated in patients (16), which is now in clinical trials (NCT05689619).

Here we report for the first time an unbiased approach to dissect the heterogeneity within metastasis-associated reactive astrocytes at the single cell level. We uncover various populations with distinct gene expression signatures suggesting previously unappreciated complexity at the functional level. Given the immediate clinical implications, we functionally dissected an immunomodulatory program present in a subpopulation within previously identified as $STAT3^+$ reactive astrocytes(16) acting on $CD8^+$ T cells. We exploit this finding to favor the efficacy of ICB in patients with brain metastases and propose a novel combined immunotherapy compatible with advanced stages of the disease and agnostic to the primary source of the metastasis. The core finding of the novel immunosuppressive mechanism demonstrated in relevant pre-clinical models and in patient-derived samples involves astrocyte derived TIMP1 binding to the CD63 receptor on $CD8^+$ T cells, which blocks their activated state. The validation of this phenotype using genetic and pharmacologic approaches allowed us to rationalize a novel combination

immunotherapy to target local immunosuppression in the brain thus, favoring complementary efforts to activate T cells systemically. Such strategy is complemented with the detection of TIMP1 in liquid biopsy to stratify those patients who could benefit the most from the combined immunotherapy.

In summary, our data not only uncover the unexplored role of reactive astrocytes as modulators of T cell function in brain tumors by dissecting disease-associated glial heterogeneity, but also exploit its functional implication on modulating brain infiltrating T cells. We report the potential of developing organ-specific immunotherapies by dissecting the emerging crosstalk between two previously unconnected cell types in the tumor microenvironment.

Results

Clusters of brain metastasis-associated reactive astrocytes suggest functional diversity including immune-modulation.

As previously reported by us and others(16–20) brain metastasis-associated astrocytes are heterogeneous. However, an unbiased approach to characterize this glial cell type in this pathological context was lacking. We applied scRNAseq on melanoma brain metastasis generated by B16/F10-BrM(16) and enriched the resident glial population by ACSA2 (Fig1A), an established marker for astrocytes(21). Our approach efficiently enriched astrocytes in the single cell population (FigS1A-B) in a non-exclusive way since we detected other cell types post-sequencing (FigS1C). 7762 ACSA2+ astrocytes were profiled to identify 9 clusters (Fig1B, SuppTable1), 3 of them (clusters 3, 7 and 6) increased in the presence of brain metastasis (FigS1D, SuppTable2-3). Interestingly, cluster 3 and cluster 7 represent a previously described subpopulation of brain metastasis-associated astrocytes characterized by enrichment in STAT3 expression and activation(16) (Fig1B-C, FigS1E-F). Given the enlarged complexity within the STAT3+ subpopulation, we dissected these two clusters attending to their pathway enrichment. Interestingly, STAT3+ cluster 3 and STAT3+ cluster 7 astrocytes seem to represent functionally different subtypes with non-overlapping top enriched pathways (Fig1D-E, FigS1G, SuppTable4). When analyzing cluster 6, corresponding to a STAT3- brain metastasis-enriched astrocytes cluster, the absence of STAT3+ identity pathways (i.e., interferon-antigen presentation, extracellular matrix and cytokine/integrin signaling) was confirmed (FigS1H, SuppTable4). The functional diversity in STAT3+ clusters could be explained by the different pattern of receptors that activate STAT3, present in these subpopulations of reactive astrocytes. While cluster 3 presents the highest expression of Il6r (FigS1I-K), cluster 7 expresses growth factor receptors that are absent in cluster 3 (FigS1I-J, FigS1L). Additionally, the expression of interaction pairs between cluster 3 and 7 suggests a dynamic evolution of STAT3+ clusters that could potentially modulate each other (FigS1M, SuppTable5). STAT3+ astrocyte clusters (with high *STAT3* expression and activation of STAT3 pathways) were further demonstrated in human brain metastases by scRNAseq (Fig1F-I, FigS1M-O, FigS1P, SuppTable6, SuppTable7). Human STAT3+ brain metastasis-associated reactive astrocytes present an increased heterogeneity with a diverse set of functions that include those found in mice clusters (SuppTable8, SuppTable9, SuppTable10). Thus, our findings suggest that STAT3+ clusters include a previously described pro-tumoral component of astrocytes(22) (cluster 3 in mice and 4 in human are enriched in interferon (Fig1D, Fig1I, SuppTable2, SuppTable4, SuppTable8)), but also an unexplored compartment (cluster 7 in mice and cluster 5 in human are enriched in extracellular matrix, cytokines and interleukins (Fig1E, Fig1I, SuppTable3, SuppTable4, SuppTable9)).

Given that the link between STAT3+ astrocytes and the immune system we previously suggested(16) was reinforced through the dissection of this astrocyte subpopulation at the single cell level with the identification of various immunomodulatory molecules, we decided to functionally test this possibility. We confirmed the immunosuppressive nature of the secretome from pSTAT3+ astrocytes by interrogating CD8+ T cells *in vitro*(16) at the molecular level when incubated with the astrocyte conditioned media (Fig2A-B, FigS2A, SuppTable11). To confirm this finding *in vivo* we evaluated whether CD8+ T cells associated with brain metastasis were dependent on the presence and activity of STAT3+ astrocytes using the STAT3

inhibitor silibinin(16,23). Although other cell types could be affected by silibinin, the levels of pSTAT3 observed in astrocytes are much higher than in CD8+ T cells(16) (FigS2B), which could suggest an increased functional dependency on this pathway. Addionally, we previoulsy demonstrated that genetically engineering STAT3 loss of function in astrocytes phenocopied the pharmacological intervention(16). With this limitation in mind, we profiled the B16/F10-BrM brain metastasis-associated immune compartment, which includes CD8+ T cells (FigS2C-D) among other cell types (FigS2E), from mice treated with silibinin (Fig2C). Our findings demonstrate that pharmacological blockade of STAT3 alters specifically the proportion of T cell subpopulations in the brain, increasing those clusters expressing known cytotoxic markers (*Cxcr6, Gzmk, Gzma, Gzmb, Ccl5, Gimap7, Xcl1, Klrc1, Klrk1* and *Cd160*), which are not found upregulated in the naïve T cells cluster (Fig2D, FigS2F, FigS2G). In order to evaluate the lack of cell type specificity of the pharmacological intervention, we validated the STAT3-dependent modulation of tumor infiltrating lymphocytes (TILs) using STAT3 depleted mice in reactive astrocytes (GFAP-Cre^{ERT2}; $Stat3^{loxP/loxP}$, abbreviated as cKO^{GFAP}-*Stat3*) (16) (Fig2E). We observed a general increase of brain metastasis associated-CD8+ T cells (FigS2H-I) accompanied with the induction of Granzyme b (Fig 2F-G), which was in agreement with the strong increased of granzyme genes *Gzmb* and *Gzmk* (FigS2J-K). However, no significant alteration in Perforin and IFN-γ expressing CD8+ T cells was observed (FigS2L-M). Thus, inhibition of STAT3, using either pharmacologic or genetic interventions, in brain metastasis-associated reactive astrocytes modulates the phenotype of CD8+ T cells *in vivo*. In order to demonstrate the functional relevance of this finding, we evaluated the ability of a CD8 blocking antibody to rescue the reduced brain metastases burden in cKO^{GFAP}-*Stat3* (Fig2H). Remarkably, blocking CD8+ T cells in cKO^{GFAP}-*Stat3* mice reverted the anti-metastasis phenotype suggesting that the infiltrating immune population is actively suppressed by STAT3+ astrocytes *in vivo* (Fig2I-J, FigS2N).

TIMP1 and STAT3 in reactive astrocytes correlate with a high immune cluster classifier in human brain metastases.

Within the secretome of pSTAT3+ astrospheres(16) several candidates were previously suggested to play a role on the immunosuppressive properties of this glial cell subpopulation(16). Among them, we became particularly interested on TIMP1 because it was recently reported as one of the top deregulated proteins within the CD45- cell fraction of human brain metastases, which includes astrocytes(24). Our proteomics data(16) show high TIMP1-specific enrichment in pSTAT3+ astrospheres (FigS3A). We further prove that TIMP1 derives from the microenvironment in human brain metastases (FigS3B-C) and that its highest expression in available scRNAseq data from experimental brain metastases (FigS1C) corresponds to astrocytes when compared to other glial cells or macrophages (FigS3D). Indeed, *Timp1* expression co-localizes with pSTAT3+ astrocytes in astrospheres and in experimental brain metastasis (Fig3A), in particular with STAT3+ cluster 7 (FigS3E, SuppTable3). Furthermore, we confirmed that the major source of TIMP1 in human brain metastases are pSTAT3+ reactive astrocytes (Fig3A, FigS3F-I), where *TIMP1* highest expression is found in the cluster of astrocytes with greatest induction of STAT3 (cluster 5, FigS3J). To demonstrate the contribution of astrocytes to microenvironment-derived TIMP1, we used the genetically modified mouse model (GEMM) GFAP-Cre; Timp1loxP/loxP (for brevity, cKO^{GFAP}-*Timp1*) (25) (FigS3K-Q). We validated the absence of TIMP1 in the conditioned medium of pSTAT3+

astrospheres(16) derived from cKO^{GFAP}-*Timp1* GEMM (FigS3O-P), where we were unable to detect any influence of TIMP1 on the established phenotype of this *in vitro* surrogate for pSTAT3+ astrocytes(16) (FigS3N). Accordingly, GFAP+ pSTAT3+ brain metastasis associated-reactive astrocytes in cKO^{GFAP}-*Timp1* GEMM remain indistinguisable from wild type ones (FigS3K-M). No additional analyses were performed to characterize astrocytes in the cKO^{GFAP}-*Timp1* GEMM. Importantly, depleting *Timp1* from astrocytes decreases brain metastasis-induced TIMP1 to non-tumor levels in the cerebrospinal fluid (CSF) (FigS3Q). Finally, we confirmed the STAT3-dependency of TIMP1 *in vivo* with both cKO^{GFAP}-*Stat3* mice (FigS3O) and pharmacological inhibition of STAT3 (FigS3R-T).

As we hypothesized that STAT3+ astrocytes are major contributors to local immunosuppression, we asked whether this astrocyte population correlated with the degree of immune infiltration in the microenvironment of human brain metastases. We interrogated the expression of *STAT3* and *TIMP1* in patient samples previously profiled with transcriptomics and annotated respect to low, medium and high immune categories(26) (Fig3B, FigS4A). Remarkably, both *STAT3* and *TIMP1* expression levels were enriched among human brain metastases classified as the high immune fraction (Fig3C-D). Of note, scored samples were compatible with reporting gene expression patterns from the microenvironment compartment (FigS4B). The correlation between the genes of interest and the immune compartment was validated in a second cohort of human brain metastases (FigS4C-D, SuppTable12). This finding could suggest that the expression of *STAT3* and *TIMP1* genes is compatible with a dense immune landscape broadly speaking, which could potentially involve the ability of these fraction of brain metastases to respond to immune checkpoint inhibitors if properly stimulated. Interestingly, we realized that the definition of human samples according to the different immune categories was reproduced by a reduced gene classifier composed by genes representative of key cell types from the microenvironment including *CD8a* (for CD8+ T cells and some subsets of dendritic cells), *CD68* (for microglia/macrophages) and *ITGAX* (mainly for dendritic cells, but also for macrophages, NK cells and granulocytes) (Fig3B and FigS4E-F). The use of these reduced number of markers to assess the immune infiltration of human brain metastasis could provide a clinically-compatible assay that might be useful to stratify patients. Consequently, we develop a multiplex analysis applying the corresponding antibodies for these cell types to a cohort of 12 selected brain metastases in RENACER(27) (List of supplementary figure, supplementary tables and authors included in the RENACER signature). The selection criteria applied responded to the inclusion of samples obtained through extended neurosurgical resection (Fig3E, SuppTable13) to make sure a substantial peritumoral microenvironment, where astrocytes are exclusively located, was present (Fig3E) (15). Samples were categorized into low/ medium/ high based on the combined score of the three antibodies (Fig3F, FigS4G), which nicely correlated with the transcriptomic scoring (Fig3G). Analysis of the abundance of *TIMP1* in the microenvironment of these samples confirmed the correlation with the high immune cluster (Fig3G). Based on these findings, we hypothesized that patients with brain metastasis treated with immune checkpoint blocking antibodies, even in the presence of an immune rich microenvironment, might not benefit from this immunotherapy given the concomitant presence of a local immunosuppressive compartment (i.e., pSTAT3+ astrocytes). Although an adequate comparison with the responders is a requisite, to preliminary evaluate our hypothesis, we identified in RENACER 8 patients affected with extracranial metastases that responded to

immune checkpoint blockade systemically but that later relapsed in the brain (Fig3H, SuppTable14). Our ability to get access to these tissues from the RENACER cohort(27) allowed us to confirm the presence of pSTAT3+ reactive astrocytes enriched in *TIMP1* (Fig3H). As CD8+ T cells are present in limited numbers infiltrating the tumor core, but mainly in the peritumoral area intermingled with reactive astrocytes (FigS4H), we hypothesized that a correlation between the potential anti-tumor quality of CD8+ T cells and the distance to pSTAT3+ reactive astrocytes might exist. Interestingly, we found that this cohort of patients shows an inverse correlation between the density of pSTAT3+GFAP+ cells and granzyme positive CD8+ T cells (Fig3I-J), by focusing on areas within the range of influence of cytokines(28). Thus, our findings provide the rationale to improve responses to immune checkpoint blockade in brain metastases with high immune infiltration by targeting STAT3+ astrocyte-dependent local immunosuppression.

TIMP1 mediates brain metastasis in a CD8+ T cell-dependent manner

To address the potential contribution of astrocyte-derived TIMP1 to the immunosuppressive phenotype on CD8+ T cells (Fig2A-J) we performed *in vitro* cytotoxicity assays. CD8+ T cell cytotoxicity was analyzed using OT-I transgenic CD8+ T cells specific for the OVA-derived SIINFEKL peptide(29) and targeted B16/F10-BrM-OVA^{GFP} cells (Fig4A, FigS5A-B). As previously reported, activated CD8+ T cells cultured in the secretome of pSTAT3+ astrospheres reduced their cytotoxicity compared to pSTAT3- secretome addition, on a melanoma brain metastatic cell line(16) (Fig4B, FigS5C-D). We found that addition of TIMP1 mimics the effect of the immunosuppressive pSTAT3+ secretome (Fig4B, FigS5C-D), in the same line as described by Oelmann et al(30). In addition, pSTAT3+ astrospheres generated from cKO^{GFAP}-*Timp1* were unable to influence the cytotoxicity of activated T cells (Fig4B, FigS5C-D). These results were complemented with *in vitro* experiments with activated T cells, where anti-TIMP1 blocking antibody reverted the effect of the otherwise immunosuppressive pSTAT3+ secretome (FigS5E-G). In order to expand this finding to more relevant models we applied the blocking antibody against TIMP1 to organotypic cultures of both experimental (Fig4C) and patient-derived brain metastases *ex vivo* (Fig4D, SuppTable15) that included the surrounding microenvironment where astrocytes and T cells co-exist (FigS5H-I) (16). Remarkably, blocking TIMP1 activity correlated with reduced metastasis-derived bioluminescence that was rescued by blocking CD8+ T cells (Fig4E). Targeting human TIMP1 in eleven patient-derived brain metastasis organotypic cultures (PDOC) from different primary tumors confirmed the decrease viability of metastases (Fig4F). We further demonstrate that the phenotype was not direct on cancer cells since anti-TIMP1 blocking antibody did not significantly influence metastatic cells in isolation (FigS5J-L). Consistent with the mouse model, the reduction in the viability of human brain metastatic cells was rescued by targeting the CD8+ T cells infiltrating the PDOC in an additional cohort of seven patients (Fig4G). Remarkably, patients stratified as high immune cluster (FigS5M, SuppTable16), which we hypothesized to respond better to anti-TIMP1 blockade in PDOCs, showed a greater decrease in cancer cell viability compared to patients with limited CD8+ T cell infiltration, low levels of STAT3 and TIMP1 and similar levels of dendritic cells and macrophages markers (FigS5N, SuppTable16). To expand the involvement of TIMP1 *in vivo* we performed metastasis assays with two experimental models. A melanoma brain metastasis model(16) and a triple negative breast cancer (TNBC) model(31) were inoculated in the cKO^{GFAP}-*Timp1* GEMM(25) (Fig4H). Brains with

conditional knock-out of *Timp1* in reactive astrocytes correlated with a decreased ability of metastatic cells to survive in this organ (Fig4I-L, Fig5SO-P). Analysis of the histology showed increased numbers of anti-tumoral brain metastasis-associated CD8+ T cells infiltrating the metastasis (Fig4M-N), which strongly suggest a potential negative influence of resident glial cells on the acquired immune system at the core of local immunosuppression.

Characterization of the influence of TIMP1 in CD8+ T cells

We characterized the influence of STAT3/TIMP1 on CD8+ T cells using immunophenotyping with different coactivatory, coinhibitory markers and cytokines. Flow cytometry analysis confirmed that, according to the decrease in cytotoxicity we observed previously (Fig4B, FigS5C-D, FigS5E-G), pSTAT3+ conditioned media (CM) decreased expression of CD25 in effector CD8+ T cells (Fig5A, Fig5B-C). Furthermore, CD25 downregulation was rescued upon depletion of *Timp1* in astrocytes (Fig5B-C). Absence of TIMP1 downstream STAT3 leads to increase of CD8+ T cells expressing inflammatory cytokines (Fig5A, Fig5D) and a decrease in exhausted CD8+ T cells (Fig5A, Fig5E). Furthermore, brain metastasis-associated CD8+ T cells increased CD44 and INFγ levels, while reduced exhaustion markers when TIMP1 was depleted from reactive astrocytes *in vivo* (Fig5F, Fig5G-L). TIMP1 has been mostly studied as a regulator of MMPs(32), however its role as a ligand binding to CD63 receptor(33) has not been addressed until recently(32,34,35). We tested if TIMP1 pro-tumoral role in brain metastasis depends on its interaction with MMPs or on its cytokine activity in organotypic cultures. Only blocking TIMP1 regions non-interacting with MMPs leads to a decrease in brain metastasis (FigS6A-C). CD63 has been previously suggested as a marker of CD8+ T cell activation(36), which we reproduced *in vitro* (FigS6D). Although, we detected a trend towards an increased percentage of circulating CD8+ T cells expressing CD63 when there is systemic disease in preclinical models (FigS6E), a robust and significant increase in the surface levels of CD63 was only detected when the CD8+ T cell fraction was evaluated in established brain metastases (Fig6A, Fig6B-D, FigS6F-G) (24). Furthermore, we confirmed the presence of CD63+CD8+ T cells *in situ* in both experimental and patient-derived brain metastases (Fig6C-D). We probed the binding of astrocyte-derived TIMP1 and CD63 on the surface of CD8+ T cells in co-cultures of pSTAT3+ astrospheres and *in vitro* activated CD8+ T cells, while the culture of these two cell types independently of each other did not reproduce the binding if the two molecules (Fig6E, FigS6H). This finding was further validated *in situ* in human brain metastasis samples, detecting specific signal in proximity ligation assays (Fig6F, FigS6I). The fact that the level of CD63 receptor increases along with the activation state of CD8+ T cells (FigS6D) and that the binding of its ligand, TIMP1, triggers an immunosuppressive phenotype (Fig4B, Fig5A-E, Fig5G-L) might be suggestive of a potential paracrine immune checkpoint. To consolidate this hypothesis, we first evaluated whether CD8+ T cells from CD63-null mice(37) exhibit improved anti-tumor ability (Fig6G). Addition of wild type CD8+ T cells to organotypic cultures of established brain metastases generated with the B16/F10-BrM cell line was not sufficient to reduce significantly the viability of cancer cells (Fig6H), which reinforces the influence of the immunosuppressive microenvironment. In contrast, the absence of CD63-TIMP1 signaling when CD63 KO CD8+ T cells were added to organotypic cultures, allowed an effective T cell-mediated killing of cancer cells (Fig6H). To further confirm the differential impact of TIMP1 among $CD63^{low}$ and $CD63^{high}$ CD8+ T cells, sorted CD8+ T cells with low or high CD63 levels were

treated with CM from either wild type or cKO^{GFAP}-*Timp1* pSTAT3+ astrospheres (FigS6J-N). While CD8+/CD63^{low} T cells did not respond to the presence of TIMP1 from STAT3+ astrospheres CM, CD8+/CD63^{high} T cells increased CD44/ CD62L levels when TIMP1 was not present (FigS6L-N). Additionally, cytotoxicity genes *Gzmb* and *Gzmk* were induced in sorted brain metastasis associated-CD8+/CD63^{high} T cells when *Timp1* was depleted from reactive astrocytes (Fig6I, FigS6O). Our findings report a novel molecular crosstalk between STAT3+ reactive astrocytes and CD8+ T cells through TIMP1-CD63 leading to the decrease of the anti-tumor activity of this component of the acquired immune system infiltrating the brain. However, due to the lack of knowledge on the signaling pathways downstream of CD63 in lymphocytes upon TIMP1 binding we performed phosphoproteomics analysis to deepen our findings on T cell immunosuppression in brain metastasis. *In vitro* activated CD8+ T cells were analyzed by LC-MSMS-based proteomics after incubation with CM from pSTAT3+ astrospheres derived from wild type or cKO^{GFAP}-*Timp1* astrocytes (Fig6J, FigS7A). Lack of TIMP1 signaling on CD8+ T cells lead to a main enrichment of signatures related to T cell activation as the top finding (FigS7B, SuppTable17). Dissecting the phosphosites significantly altered when the immunosuppressive signal activated by TIMP1 was not present revealed several kinases with altered levels of their phosphorylated substrates (Fig6K, SuppTable18). Among them, we validated changes in ERK1/2 phosphorylation (pERK1/2) in CD8+ T cells infiltrating metastases when targeting TIMP1 in astrocytes (cKO^{GFAP}-*Timp1*) (Fig6L, FigS7C). Furthermore, analysis of human brain metastases scored with multiplex (Fig3E-G) showed a correlation between the quality of infiltrating CD8+ T cells regarding their pERK1/2 status and their immune cluster category (Fig6M, FigS7D, SuppTable19). Finally, we validated the modulation of ERK activity using rTIMP1 or anti-TIMP1 on CD8+ T cells while incubated in astrospheres conditioned medium (FigS7E). Overall, we report that signaling downstream of CD63 receptor has major implications in anti-tumor activity of CD8+ T cells upon TIMP1 binding through the modulation of multiple kinases including ERK1/2 (Fig6N).

A combined immunotherapy targeting local immunosuppression provides superior control of brain metastasis.

In order to demonstrate the therapeutic implications of our findings we decided to test whether inhibition of STAT3 could be combined with immune checkpoint blockade (ICB) to obtain better anti-tumor responses in the brain (Fig7A). The B16/F10-BrM model responded to anti-PD1/ anti-CTLA4 extracranially (Fig7B, FigS8A) but did not decrease tumor burden in the brain (Fig7B, FigS8B). Complementary, as previously reported(16), the STAT3 inhibitor silibinin achieved a significant control of brain metastases (Fig7B, FigS8B) but with limited extracranial benefit (Fig7B, FigS8A). Although brain bioluminescence imaging (BLI) *ex vivo* did not show any additional benefit of the ICB and silibinin combination beyond the response to silibinin monotherapy (FigS8B), histological examination of these brains demonstrated that the response was clearly superior (Fig7C, SuppTable20). Interestingly, although large metastases were mainly controlled by silibinin, metastases of medium size were more effectively targeted by ICB with the combination therapy (Fig7C, SuppTable20). The apparent dissociation between BLI and histology might suggest that the data obtained with bioluminescence is mainly contributed by large lesions, thus lacking the sensitivity to score changes affecting metastases from other size categories. In fact, we previously reported that silibinin was not effective against smaller metastasis both in experimental models and

patients since STAT3+ reactive astrocytes are not present(16). We hypothesized that the combined immunotherapy including silibinin could sensitize experimental metastases to the attack of CD8+ T cells activated systemically with ICB. Accordingly, we evaluated whether the anti-tumor response was increased when targeting local immunosuppression with silibinin in the brains of ICB treated mice. Histological analysis of the brains from mice treated with the combined immunotherapy showed increased markers of cytotoxic activity (Fig7D-E) and cleaved caspase 3-staining in cancer cells (FigS8C-D). In order to reinforce our finding, to discard any influence of extracranial metastasis in the brain phenotype(11) and to explore the potential additional benefit of a combination with radiotherapy, we repeated the combination therapy using intracranial injection in this model to apply local therapy (Fig7F), as previously reported(31). Since the B16/F10-BrM model lacks a recently described radioresistance mechanism(31), we found it does respond to fractionated radiotherapy (FigS8E). Accordingly, we added ICB and silibinin to irradiated mice and scored whether any additional benefit in overall survival was detected beyond what is provided by the local therapy. In this experimental setting, ICB showed a superior ability to target brain metastases mimicking the effect of silibinin (FigS8F). More importantly, the triple combination therapy did add additional brain tumor control increasing overall survival (Fig7G, FigS8F). Consistently, the combined immunotherapy led to a more efficient cancer cell killing (Fig7H-I) and more proliferative CD8+ T cells locally (Fig7J-K). To expand our finding to other relevant preclinical models and test whether the improved control of brain metastasis when combining ICB and STAT3 inhibition was triggered by impairing TIMP1-mediated immunosuppression, we used the cKO^{GFAP}-*Timp1* mice intracardially injected with E0771-BrM cells and treated with ICB (FigS8G). We found that abolished secretion of the STAT3 downstream target TIMP1 in reactive astrocytes improved ICB benefit in brain metastasis (FigS8H-J), affecting both metastases of medium and big size (FigS8K-L, SuppTable20).

Our initial findings suggest the feasibility of using TIMP1 to stratify patients that could benefit from the combined immunotherapy (Fig3D). However, a systemic treatment should not rely on a biomarker requiring neurosurgery to score tissue samples. Consequently, given the secretory ability of STAT3+ RA(16), which includes TIMP1 (FigS3A), together with existing reports using astrocyte-derived biomarkers in liquid biopsies(38,39), we evaluated such possibility in patients with brain metastasis. The cerebrospinal fluid (CSF) has been suggested as a better surrogate to the brain parenchyma than blood(40–43), so we decided to evaluate TIMP1 in these two types of liquid biopsies from the RENACER cohort. While TIMP1 levels in the blood did not differ from healthy controls individuals (FigS9A, SuppTable21), the CSF from patients with brain metastasis was significantly enriched in the potential biomarker (Fig7L, SuppTable21). Furthermore, high levels of TIMP1 in CSF of brain metastasis patients predicts worse overall survival (FigS9B, SuppTable22). In order to evaluate the correlation between the biomarker and the susceptibility to respond to strategies that block local immunosuppression, we checked whether any of these patients also had PDOC established from extended neurosurgeries as part of the RENACER pipeline(27). A selected group of samples with confirmed presence of immune cells compatible with medium-high immune clusters (Fig3G, FigS9C-D, SuppTable21, SuppTable23-25) with PDOC and values of TIMP1 in the CSF above the mean of healthy controls could be allocated. According to the data reported above, PDOC proved their sensitivity to the blocking anti-TIMP1 antibody (Fig4F, Fig7M, Fig7N, FigS9C, SuppTable15, SuppTable21) in a CD8+ T cell dependent manner (Fig4G).

Thus, our data provides the rationale to test a novel combined immunotherapy consisting on ICB antibodies and silibinin as a strategy to maximize the access to metastases and anti-tumor activity of CD8+ T cells by blocking local immunosuppression. In addition, the therapeutic strategy described could potentially be guided by a biomarker compatible with liquid biopsy to improve patient stratification and evaluation of the therapeutic benefit. Overall, our finding represents the first comprehensive approach to target symptomatic brain metastases with a biomarker-guided immunotherapy.

Discussion

Recent clinical trials have tested ICB antibodies in patients with brain metastasis derived from melanoma and lung cancer(2–8). The results indicate variable rates of positive responses that could oscillate between 0-60% of the patients. However, positive response rates were mainly attributable to asymptomatic brain metastasis, which tend to be smaller in size. Indeed, in those trials where symptomatic brain metastases were considered, ICB benefits for intracranial lesions dropped significantly(2,7), which has created concerns regarding their translation to real world clinical practice(44). Although corticoids have been suggested to underlie this differential responses among patients it remains controversial(7,12–14,45).

The data reported here could potentially explain these clinical findings to some extent since our previous observations concluded that pSTAT3+ reactive astrocytes are not present in early but in advanced stages of the disease(16) and patients treated with silibinin, a STAT3 inhibitor(16,23), decreased the size of the metastasis to a certain point, which then remain stable(16). Thus, we conclude that the lack of local benefit from ICB in patients with symptomatic brain metastasis reflects, rather or in addition to a potential consequence of the use of corticoids, a pSTAT3+ reactive astrocytes-driven mechanism that is responsible for local immunosuppression affecting CD8+ T cells arriving from the periphery. Thus, although ICB might facilitate the access of active T cells into the brain, these potential cellular anti-tumor entities suffer the local immunosuppressive environment that might underlie the requirement of a combination therapy.

Our data indicates that, the presence of brain metastasis alters the immune landscape in the brain increasing immune cells numbers, however brain metastasis-associated T cells remain ineffective to target cancer cells. By dissecting astrocyte heterogeneity, we found subpopulations of astrocytes enriched in potential immunomodulatory signatures. When exploring the molecular basis of immunomodulation mediated by metastasis-associated astrocytes, we found that the STAT3-dependent gene *TIMP1*, previously reported as a top differentially expressed protein in human brain metastasis samples(24), imposes a local immunosuppressive hub affecting the quality of CD8+ T cells. We demonstrate that the main source of TIMP1 is in the tumor microenvironment, and specifically a subpopulation of reactive astrocytes. TIMP1 has been mostly considered an MMP inhibitor(32). However, TIMP1 also plays an MMP-independent role by binding to CD63(32–35,46). We report a novel function for TIMP1/CD63 on the surface of CD8+ T cells infiltrating brain metastasis mediating immunosuppression in an antigen dependent and independent manner. Although the acquired immune system is necessary for STAT3/TIMP1-mediated immunosuppression, considering the non-restricted expression of CD63 on CD8+ T cells, it could be presumed that extracellular vesicles expressing CD63 and other cell types such as macrophages, may be also affected by TIMP1 increased in the brain metastasis microenvironment. The potential

involvement of this and other immune cell types including dendritic cells that are also directly affected by STAT3 inhibition in reactive astrocytes or as a consequence of the improved immune landscape, should be further addressed. Additionally, although our genetic strategy confirmed that STAT3 inhibition with silibinin is recapitulated with an astrocyte-specific targeting approach on STAT3; we cannot fully discard that the pharmacological strategy is also affecting other cell types. Whether the immunosuppressive role of the reactive astrocyte subpopulation could play a role in other brain disorders remains to be addressed. Indeed, it is tempting to speculate that given the role of astrocytes to limit potential threats to the brain, this could include their ability to block infiltrating T cells, which might otherwise increase the risk of causing deleterious consequences in this low regenerative organ.

Given that silibinin targets pSTAT3+ reactive astrocytes(16) we propose that the combination with ICB will increase local responses by facilitating CD8+ T cell anti-tumor activity in patients with brain metastasis. It should be noted that, silibinin could be affecting systemic T cells and its effects may be potentiated by the action of radiotherapy-promoted T cell priming(47). Even more, the fact that the levels of STAT3 and TIMP1 are enriched in those patients where the local environment is compatible with a potential response to ICB (i.e., high immune cluster) justifies the use of TIMP1 as a potential biomarker. CSF liquid biopsy to detect TIMP1 would allow not only selecting the patients who would benefit the most from the combined immunotherapy, but also to follow the therapeutic response over time.

Overall, our study demonstrates that dissecting the heterogeneity within the metastasis-associated microenvironment to cell type specific subpopulations defined functionally (i.e., mouse cluster 7 and human cluster 5 within STAT3+ reactive astrocytes) offers the possibility to develop novel therapeutic vulnerabilities. By exploring a specific crosstalk within the altered brain metastasis microenvironment (TIMP1 ligand binding to CD63 receptor) we might have contributed to clarify an unsolved clinical limitation (i.e., lack of response in symptomatic brain metastases). Given the preliminary data that we show in patients, the rationale of combining silibinin with ICB as a more effective immunotherapy for brain metastases supports a follow-up clinical trial after completing the one currently ongoing with silibinin as monotherapy (NCT05689619).

Acknowledgments

We thank all members of the Brain Metastasis Group, A. Schietinger, A. Gros and A. A. Boire for critical discussion of the manuscript and the CNIO Core Facilities for their excellent assistance, especially the Monoclonal Antibodies Core Unit that provided us with the following plasmids: PCMV6-hTIMP1-myc-DDK, PCDNA3.1-mTIMP1, PCDNA3.1-mTIMP2, PCDNA3-hTIMP3 and PCMV6-mTIMP3-myc-DDK. We thank Euromed as a supplier of Silymarin for *in vivo* experiments. We thank D. Sancho (CNIC) and the members of the Melanoma Group from CNIO for Tg(TcraTcrb)1100Mjb/J mice, the OVA-OT-I system and their help with cytolysis assays. We want to particularly acknowledge the patients and the Biobank Nodo Hospital Virgen Macarena (Biobanco del Sistema Sanitario Público de Andalucía) integrated in the Spanish National biobanks Network (PT20/00069) supported by ISCIII and FEDER funds, for their collaboration in this work. This study was funded by MINECO (SAF2017-89643-R, SAF2014-57243-R, SAF2015-62547-ERC) (M.V.), Fundació La Marató de TV3 (141) (M.V., A.C.), Fundación Ramón Areces (CIVP19S8163) (M.V.) and (CIVP20A6613) (E.O.), H2020-FETOPEN (828972) (M.V.), Cancer Research Institute (Clinic and Laboratory Integration Program CRI

Award 2018 (54545) (M.V.), LAB AECC 2019 (LABAE19002VALI) (M.V.), ERC CoG (864759) (M.V.), ERANET-TRANSCAN-3 (TRANSCAN2021-2023) (M.V.) with funds from Instituto de Salud Carlos III/ NextGenerationEU/ PRTR (AC20/00114) and FC AECC (TRNSC213878VALI), Federal Ministry of Education and Research (03ZU1111LB) and co-funded by the European Commission (01KT2304B) (M.S.), MICINN (PID2019-107956RA-I00) (A.P.), LAB AECC 2021 (LABAE211744PALA) (A.P.), ERC StG (804236) (A.P.), NIH-NS078392 (S.J.C.), La Caixa INPhINIT Fellowship (LCF/BQ/DI19/11730044) (A.P.-A.), MINECO-Severo Ochoa PhD Fellowship (BES-2017-081995) (L.A.-E.) and an AECC postdoctoral fellowship (POSTD19016PRIE) (N.P.), Gobierno Vasco predoctoral fellowship (PRE_2019_1_0320) (B.J-L), FPI predoctoral fellowship (PRE2020-092342) (P. V-B.), Ramón y Cajal fellowships: RYC2018-024183-I (A.P.) and RYC2022-038084-I (D.S), M.V. is an EMBO YIP member (4053). CNIO is supported by the ISCIII, the Ministerio de Ciencia e Innovación, and is a Severo Ochoa Center of Excellence (SEV-2015-0510).

Author contributions

N.P.: Conceptualization; Data curation; Formal analysis; Validation; Investigation; Visualization; Methodology; Writing-original draft; Writing-review and editing. A.P-A., M.P-G., V.P., L.A-E., A.R., O.S., D.S., B.J-L., L.E-M.: Formal analysis; Investigation; Visualization; Methodology. C.H-O., S.G-M., O.G-C.: Data curation; Formal analysis; Methodology. P.V-B.: Data curation; Formal analysis; Investigation; Methodology. L.R.,A.S.: Data curation; Formal analysis; Investigation; Visualization; Methodology. E.C.: Formal analysis; Supervision; Visualization; Methodology. F.G.: Data curation; Formal analysis; Investigation; Methodology. A.S., S.G-M., R.S-P.: Formal analysis; Supervision; Validation. E.M-S., A.P-N., A.H-L.: Human samples and clinical evaluation. S.J.C.: provided the Timp1loxP/loxP mice. P.S.: provided the CD63-null mice. M.S.,A.C-C.,A.P.: Resources, Formal analysis; Supervision; P.B., V.C., C.S., D.A., N.A., M-J.A., E.O-P., A.G., C.F., A. de la L., A.L., A.D., P.D., M.P., A.D-P., SH.N-C., C.B., G.P., B.E., I.G., S.A., A.P., A.H., O.T., R.G., JA.F., G.B., L.B., A.P., R.D., P.C., L.M., R.S., S.C.C., E.M., M.M., M-S-O., A.R., F.M., S.RyC., M.S.F., L.F.: Supervision; provided and processed the human samples and collected clinical data; M.V.: Conceptualization; Resources; Project administration; Formal analysis; Supervision; Funding acquisition; Validation; Investigation; Visualization; Methodology; Writing-original draft; Writing-review and editing.

Material and methods

Animal studies

All animal experiments are in accordance with a protocol approved by the CNIO, Instituto de Salud Carlos III and Comunidad de Madrid Institutional Animal Care and Use Committee (IACUC.030-2015, CBA35_2015-v2 and PROEX135/19). The cKO^{GFAP}-*Stat3* model was generated by breeding GFAP-CRE/ERT2 (B6.Cg Tg(GFAP-cre/ERT2)505Fmv/J, Jackson Labs, ref. 012849) with STAT3loxP/loxP, cKO^{GFAP}-*Timp1* was generated as described by Sutter et al(25) and CD63-null mice was generated as described by Schröder et al(37). Tg(TcraTcrb)1100Mjb/J (OT-I mice) were kindly provided by D. Sancho (CNIC) for the isolation of OT-I T cells.

Brain colonization assays were performed in 10-15 weeks old mice, both males and females (except for the E0771-BrM cells that were injected in females), as previously described(16) by injecting 100 µl of PBS into the left ventricle containing 100,000 cancer cells or 1 µl of PBS intracranially (right frontal cortex, approximately 1.5 mm

lateral and 1 mm caudal from bregma, and to a depth of 2 mm) containing 40,000 cancer cells by using a gas-tight Hamilton syringe and a stereotactic apparatus.
Brain colonization was analyzed *in vivo* and *ex vivo* by bioluminescence imaging (BLI). Mice were anesthetized with isofluorane and injected retro-orbitally with D-Luciferin (150 mg/kg) and imaged with IVIS® Spectrum and Lumina III In Vivo Imaging System (Caliper Life Sciences). Bioluminescence analysis was performed using Living Image software, version 64. *Ex vivo* values at the endpoint were normalized to the BLI values of the head *in vivo* three days after injection of the cancer cells before starting treating with the different drugs. Tamoxifen (I.p., 1 mg/day) was administered three days after cancer cells inoculation until the end of the experiment, Silibinin in the formula of Silymarin 77.5% (Euromed, Code No. 345316.00) was administered by oral gavage daily (200 mg/kg) three days after cancer cells inoculation and treatment continued until mice reached the endpoint of the experiment. Starting three days after cancer cells inoculation, Control IgG (i.p; 10 mg per kg, BioXcell, ref. BE0090), Anti-CD8α (i.p; 10 mg per kg, BioXcell, ref. BE0061), Anti-PD1 (i.p; 10 mg/ kg BioXcell, ref. BE0146) and Anti-CTLA4 (i.p; 10 mg/ kg, BioXcell, ref. BE0032) antibodies were administrated every two days during the first two weeks of treatment and in non-consecutive days during the last week of treatment.

Radiotherapy

Three days after intracranial injection of B16/F10-BrM cells, the presence of established brain metastases was confirmed by BLI. WBRT protocols mimicking the clinical procedure were applied as previously described(31): fractionated dose of 3 Gy per day for 5 consecutive days or completed regimen with 3 Gy per day for additional 5 days after 2 days without irradiation. Mice were followed up by BLI until the humane endpoint was reached.

Brain slice assays

Organotypic slice cultures from adult mouse brain were prepared as previously described(16). Organotypic cultures included brains obtained at the endpoint of metastatic disease when brain lesions are established. Brains were dissected in Hank's balanced salt solution (HBSS) supplemented with HEPES (pH 7.4, 2.5 mM), D-glucose (30 mM), CaCl2 (1 mM), MgCl2 (1 mM), NaHCO3 (4 mM), and embedded in low-melting agarose (Lonza) preheated at 42° C. The embedded brains were cut into 250 µm slices using a vibratome (Leica). Slices were divided at the hemisphere into two pieces. Brain slices were placed with flat spatulas on top of 0.8 µm pore membranes (Sigma Aldrich) floating on slice culture media (Dulbecco's modified Eagle's medium (DMEM), supplemented HBSS, fetal bovine serum 5%, D-glucose (30 mM), L-glutamine (1 mM), 100 IU/ml penicillin, 100 mg/ml streptomycin). BLI was acquired after generating brain slices (Day 0) to confirm the presence of brain metastasis and 3 days after the addition of the inhibitor (Day 3) considering for analysis floating brain slices. Growth rate was obtained by comparing fold increases between day 3 and day 0. In the case of T cell addition, 20,000 CD8+ T cells were seeded on the top of established brain metastasis brain slices after one day in culture. Control IgG (10 µg/ml, BioXcell, ref. BE0090) or preservative (0.05% Sodium azide) was added in the control condition if necessary, Anti-TIMP1 antibody (102D1) (10 µg/ml, Thermofisher, ref. MS608PABX), Anti-TIMP1 (N-terminal) (10 µg/ml, Sigma Aldrich, ref. SAB2109118), Anti-TIMP1-Carboxyterminal end (10 µg/ml, Abcam, ref. ab38978), and Anti-mouse CD8α (100 µg/ml, BioXcell, ref. BE0061)

were added to the media at day 0. Brain slices were fixed in paraformaldehyde (4%) overnight followed by free-floating immunofluorescence.

Cell culture

Mouse brain metastatic cell lines have been generated as previously described(16,31). All cell lines were tested negative for Mycoplasma (by qRT-PCR). We did not do cell authentication beyond visual, morphological and growth rate analyses. The maximum number of passages between thawing and use are 15 for all the cell lines.

B16/F10-BrM were cultured in DMEM media supplemented with 10% fetal bovine serum (FBS), 2 mM L-Glutamine, 100 IU/ml penicillin/streptomycin and 1 mg/ml amphotericin B, E0771-BrM were cultured in RPMI1640 medium supplemented with 10% FBS, 1% HEPES, 2 mM L-glutamine, 100 IU/ml penicillin/streptomycin and 1 mg/ml amphotericin B. B16/F10-BrM-OVA^{GFP} cells were generated by lentiviral-mediated transduction of a truncated non-secreted ovalbumin (OVA)-GFP fusion protein (bm1 T OVA) generously supplied by D. Sancho (CNIC). HEK 293T cells (cultured in DMEM media supplemented with 10% FBS, 2 mM L-glutamine, 100 IU/ml penicillin/streptomycin and 1 mg/ml amphotericin B) at 70% confluence were transfected in Opti-MEM with Lipofectamine 2000 (Invitrogen) and incubated at 37°C overnight with the corresponding plasmids. Mouse astrocytes were obtained from one to three-day old pups(16). Brains were mechanically dissociated, filtered through 70 µm filters and cell suspension was cultured in a petri dish for the next seven days. After gentle shaking at 37 °C overnight, the media was changed.

Astrosphere assays

Astrospheres were generated as previously described(16). Briefly, mouse astrocytes were obtained from mechanical dissociation of brains from 1- to 3-day-old pups. After 7 days in culture and gentle shaking overnight at 37 °C, the media was changed and astrocyte enrichment was confirmed. Astrocytes were treated with a cytokine cocktail including EGF (0.01 µg/ml, R&D Systems, ref. 2028-EG-200), MIF (0.1 µg/ml, R&D Systems, ref. 1978-MF-0257CF) and TGFα (0.1 µg/ml, R&D Systems, ref. 239-A-100) in DMEM media with B27 (1x) for 96 hours. After treatment, 5x104 astrocytes were seeded in low attachment plates and incubated for seven days in the presence of the same media to evaluate the ability to form astrospheres. Conditioned media was collected, filtered and added to activated CD8+ T cells.

Immunoblotting

Lysis buffer (Cell Signaling ref. 9803S) with the following protease inhibitors: 200 mM Na3VO4, 500 mM NaF, 100 mM PMSF, was used to extract total protein. Protein lysate from the microenvironment was obtained by dissecting Luciferase- tissue immediately adjacent to Luciferase+ cancer cells. Microdissection was initially validated by confirming the absence of GFP+ cells using flow cytometry. Tissue was mechanically desegregated with the FastPrep-24™ 5G lysis system (MPBiomedical) by using zirconium beads at 6.0 m/s for 15 s followed by 10 min incubation on ice before lysis. For protein quantification, BCA protein color kit was used (Fisher Scientific, ref. 23227). After denaturalization, 10-50 ug of protein lysates were resolved by SDS-PAGE. Transfer to PVDF membranes (VWR, ref. 10600021) was carried out in transfer buffer 1X (Alaos, ref. TT5C-10) 20% methanol for 2 hr 100V. Blocking was performed with 5% milk and membranes were washed with TBS-Tween 0.1 %. The following primary antibodies: p44/42 MAPK (Erk1/2) (1:1000, Cell

Signaling, ref. 9107), Phospho-p44/42 MAPK (Erk1/2) (1:1000, Cell Signaling, ref. 4370), Anti-TIMP1 (1:1000, Thermofisher, ref. MS608PABX), Anti-CD63 (MX-49.129.5) (1:500, Santa Cruz, ref. sc-5275), Anti-Tubulin (1:5000, Santa Cruz, ref. sc-17787), Anti-vinculin (1:10000, Sigma, ref. V9131) and secondary antibodies from Invitrogen (AF680) and LiCor Odissey CLx system were used for visualization.

Immunoprecipitation

For immunoprecipitation, co-cultures of STAT3+ astrospheres (as described above) and CD8+ T cells (cultured *in vitro*) were performed. CD8+ T cells were added over STAT3+ astrospheres (washed with PBS 1X after gently centrifugation) in a concentration of 6x105 CD8+ T cells/1.5 ml of co-culture. After 72 hours in culture, 1000 µg of total protein extract was incubated at 4 ºC overnight with Anti-CD63 (MX-49.129.5) (Santa Cruz, ref. sc-5275), or isotype control (IgG1, Cell Signaling, ref. #5415) in a concentration of 10 µg/mg of protein. Dynabeads protein-G (Thermofisher, ref. 10003D) were vortexed and washed twice. Then, 50 µl were incubated with the different fractions for 2 hours at 4 ºC. Finally, samples were washed and eluted for detection of CD63 and TIMP1 by immunoblotting.

RNA isolation and cDNA synthesis

QIAshredder columns (QIAGEN) were used to homogenize the preparation when needed and whole RNA was isolated using the RNAeasy Mini Kit (QIAGEN) (human and mouse tissue) or PicoPure RNA isolation Kit (ThermoFisher) (CD8+ T cells). 150-1000 ng RNA was used to generate cDNA using iScript cDNA Synthesis Kit (Bio-Rad, ref. 1708890). cDNA from sorted cells was amplified with SsoAdvanced PreAmp Supermix (Bio-Rad, ref. 1725160).

qRT-PCR

Gene expression was analyzed using SYBR green gene expression assays (GoTaq® qPCR Master Mix Promega, ref. A6002). The following mouse genes were used (5´->3´, forward;reverse):
Actin (GGCACCACACCTTCTACAATG; GTGGTGGTGAAGCTGTAGCC),
Timp1 (GAGACACACCAGAGCAGATACC; TGGTCTCGTTGATTTCTGGGG),
Gzmk (GCCATTTATGGCGTCCATCC; CCGGACTGAAGTCGTGAGAA),
Gzmb (CAGGAGAAGACCCAGCAAGTCA; CTCACAGCTCTAGTCCTCTTGG),
S100b (CTGGAGAAGGCCATGGTTGC; CTCCAGGAAGTGAGAGAGCT),
Itgam (AAGCAGCTGAATGGGAGGAC; TAGATGCGATGGTGTCGAGC).
Quantitative PCR reaction was performed on QuantStudio 6 Flex Real-Time PCR System (Applied Biosystems) and analyzed using the software QuantStudio 6 and 7 Flex Software.

Bulk RNA-seq

Total RNA samples (500 ng), with RNA Quality score of 9.4 on average (range 9.0-9.8 on a PerkinElmer LabChip analyzer), were converted into sequencing libraries with the "NEBNext Ultra II Directional RNA Library Prep Kit for Illumina" (NEB #E7760). Briefly, polyA+ fraction is purified and randomly fragmented, converted to double stranded cDNA and processed through subsequent enzymatic treatments of end-repair, dA-tailing, and ligation to adapters. Adapter-ligated library is completed by PCR with Illumina PE primers. The resulting purified cDNA libraries were applied to an Illumina flow cell for cluster generation and sequenced on an Illumina NextSeq 550 (with v2.5 reagent kits) by following manufacturer's protocols. Raw images

generated by the sequencer are submitted to analysis, per-cycle basecalling and quality score assignment with Illumina's RTA (Real Time Analysis) integrated primary analysis software. Conversion of BCL (base calls) binary files to FASTQ format is subsequently performed with Local Run Manager GenerateFASTQ Analysis Module (Illumina). Eightysix-base-pair single-end sequenced reads followed adapter and polyA tail removal as indicated by Lexogen. Mouse reads were analysed with the Nextpresso (https://doi.org/10.2174/1574893612666170810153850) pipeline as follows: sequencing quality was checked with FastQC v0.11.0 (https://www.bioinformatics.babraham.ac.uk/projects/fastqc/). Reads were aligned to the mouse genome (GRCm39) with TopHat-2.0.10(48) using Bowtie 1.0.0(49) and Samtools 0.1.19(50), allowing 3 mismatches and 20 multihits. The Gencode vM26 gene annotation for GRCm39 was used. Read counts were obtained with HTSeq(51). Differential expression and normalization were performed with DESeq2(52), filtering out those genes where the normalized count value was lower than 2 in more than 50% of the samples. From the remaining genes, those that had an adjusted p-value below 0.05 FDR were selected.

Immunofluorescence and immunohistochemistry

For immunofluorescence, fixation with PFA 4% at 4° C was applied to tissue prior to slicing of the brain by using a vibratome (250 µm slices) (Leica) or sliding microtome (80 µm slices) (Fisher). Both types of brain slices were blocked in NGS 10%, BSA 2%, Triton 0.25% in PBS for 2 hours at room temperature (RT). Primary antibodies: Anti-KI67 (1:500, Abcam, ref. ab15580, 1.500), Anti-HMB45 (1:500, Abcam, ref. ab732), Anti-CD63 (1:100, Santa Cruz, ref. sc-5275), Anti-GFAP (1:1000, Millipore, ref. MAB360), Anti-GFP (1:1000, Aves Labs, ref. GFP-1020), Anti-cleaved-caspase-3 (1:500, Cell Signaling, ref. 9661), Anti-CD8 (1:100, Novus Biologicals, ref. NB200-578), Osteopontin (1:100, Santa Cruz, ref. 21742) and Anti-MHC Class 1 H2 Db/H2-D1 (1:100, Abcam, ref. ab25244) were incubated overnight at 4 ºC in blocking solution and the following day for 30 min at RT. After washing in PBS-Triton 0.25%, secondary antibodies: Alexa-Fluor Anti-chicken488, Anti-chicken647, Anti-rabbit555, Anti-mouse555, Anti-mouse488, Anti-mouse647, Anti-rat555 and Anti-rat488 (Invitrogen, dilution 1:300) were added in blocking solution and incubated for 2 hours. After washing in PBS-Triton 0.25%, nuclei were stained with bisbenzimide (1 mg/ml; Sigma) for 7 min at RT.

Immunohistochemistry of paraffin embedded tissues was performed at the CNIO Histopathology Core Facility. For the different staining methods, the slides were deparaffinized in xylene and rehydrated by a graded ethanol series to water. Several immunohistochemical reactions were performed on an automated immunostaining platform (AutostainerLink 48, Agilent; Discovery XT-ULTRA, Ventana-Roche).

First, antigen retrieval was performed with the appropriate pH buffer and endogenous peroxidase was blocked (3% hydrogen peroxide). The slides were then incubated with the appropriate primary antibody, as detailed in Supplementary Table 23, for single, double or triple staining. Following the primary antibody, the slides were incubated with appropriate secondary antibodies and with horseradish peroxidase conjugated visualization systems when needed.

The immunohistochemical reaction was revealed using ChromoMap DAB, Discovery Purple or Teal Kit (Ventana, Roche). Nuclei were counterstained with hematoxylin. Finally, slides were dehydrated, rinsed and mounted for microscopic evaluation. Positive controls for primary antibodies were included in each staining series.

Lysozyme immunohistochemistry and RNAScope staining method were perform in an automated immunostaining platform (Ventana Discovery ULTRA, Roche), including deparaffination and re-hydrated as a part of the platform protocol with the appropriate probe: Tissue inhibitor of metalloproteinase 1(TIMP1) mRNA (ACD, ref. 567849 for human and ACD, ref. 316849 for mouse). After the probe, slides were incubated with the corresponding Probe Amplification kit (RNAScope VS Universal HRP Detection Reagent, ACD, ref. 323210), conjugated with horseradish peroxidase and reaction was developed using 3, -diaminobenzidine tetrahydrochloride (DAB Detection Kit, Ventana, Roche, ref. 760-224).

Proximity ligation assay

Interaction between CD63 and TIMP1 was investigated using *In situ* Duolink (Duolink® In Situ Orange Starter Kit Mouse/Rabbit, ref. DUO92102) according to manufacturer´s instructions. Paraffin sections were deparaffinized, and antigen retrieval was done by HIER in citrate buffer high pH. Next, sections were blocked for one hour at 37 ºC and incubated with Anti-TIMP1 antibody (1:1000, Dako, ref. M6793) and Anti-CD63 antibody (1:500, Sigma, ref. HPA010088) for 30 min at 37 ºC. Proximity ligation assay probes were added, and the sections were incubated for one hour at 37 °C followed by ligase oligonucleotides added for 30 min at 37 °C. Finally, amplification solution was added for 100 min at 37 °C. Then, slides were incubated with Anti-GFAP (1:500, Abcam, ref. ab4674) and Anti-CD8 (1:100, Novus Biologicals, ref. NB200-578) antibodies for one hour at room temperature (RT) followed by several washes and incubation for one hour at RT with secondary antibodies (Invitrogen, dilution 1:300). Coverslips were mounted using DAPI to visualize cell nuclei. Only primary antibodies or omission of primary antibodies were used as negative controls.

Image acquisition and analysis

Sample selection for analysis was done based on expert histopathological evaluation.

Images were acquired with a Leica SP5 up-right confocal microscope 10X, 20X, 40X and 63X objectives and analyzed with ImageJ software. Whole slides were acquired with a slide scanner (AxioScan Z1, Zeiss) and images were captured with Zen Blue software (V3.1 Zeiss). Human samples were analyzed with QuPath(53).

Multiplex immunohistochemistry

To investigate the immune architecture of human and murine brain metastases, we employed Opal technology (Akoya Biosciences, Menlo Park, CA, USA) which allows simultaneous imaging of several markers within one tissue section. The staining was performed on a Ventana Discovery Ultra instrument (Ventana Medical Systems, Basel, Switzerland) and imaged using the Vectra 3 automated quantitative pathology imaging system (Akoya Biosciences) as described previously(54). In brief, FFPE samples were deparaffinised, rehydrated, and subjected to heat-mediated antigen retrieval for 32 min at 95 °C in cell conditioning solution (CC)1 (Ventana Medical Systems, pH9). Upon incubation of the primary antibody according to Supplementary Table 24, the matching horseradish peroxidase (HRP)-coupled secondary OmniMap antibody (Ventana Medical Systems) was added for 12 min at 36 °C. Following, the signal was detected by incubation of the matching Opal fluorophore (Akoya Biosciences) for 8 min at RT. Afterwards, the antibody complex was removed by heat-mediated stripping with CC2 buffer (Ventana Medical Systems, pH6) for 24 min

at 100 °C. The incubation of primary antibody, secondary antibody, fluorophore and subsequent heat treatment was repeated until all markers were detected. Finally, nuclei were counterstained with DAPI (Merck, Darmstadt, Germany) and slides were mounted with a coverslip using fluoromount G medium (SouthernBiotech, Birmingham, Alabama, USA). After whole-scanning (x100) of sections using the Vectra 3.0 Automated Imaging System (Akoya Biosciences), regions of interest were defined in Phenochart™ software (Akoya Biosciences) and multispectral images (MSIs) were acquired (x200 magnification). The imaging data was then quantified using inForm (Akoya Biosciences) and R software. Briefly, MSIs were unmixed using a previously built library consisting of single stained tissue slides for all used fluorophores and DAPI. Subsequently, tissue segmentation and cell segmentation were performed. For quantification of stained cells, a self-learning approach was applied to phenotype all cell types. The downstream analyses were performed in R software using the add-ins phenoptr and phenoptrReports (Akoya Biosciences).

Single-cell RNA sequencing

Mouse brains were extracted in pre-cooled D-PBS 1X and were processed with the Adult Brain Dissociation Kit (Miltenyi, ref. 130-107-677) using gentleMACS C Tubes (Miltenyi, ref. 130-093-237) and the gentleMACS™ Octo Dissociator (Miltenyi, ref. 130-096-427). Cell suspension was filtered with a 70 µm strainer and was centrifuged at 300 g for 10 min at 4 °C. For myelin removal, the protocol described by Korin et al(55) was followed. Pellet was resuspended with 7 ml of RPMI-1640, at room temperature and 3 ml of SIP solution (Stock isotonic Percoll, ref. GE17-0891-02 Sigma Aldrich) was added to each tube mixing gently. Gradually the 30% (vol/vol) percoll/cell mixture was layered on top of 2ml of 70% (vol/vol) SIP in PBS 1X. Samples were centrifuged at 500g, 30 min, 18 °C, with minimal deceleration. The top layer of myelin was removed using a 10 ml pipette and the solution containing all cellular fractions was centrifuged at 500g, 7 min, 18 °C. The supernatant was discarded and the cells ready for staining were diluted in cold D-PBS/BSA buffer 0.5%. Cell suspension was magnetic labelled with Anti-ACSA-2 (Miltenyi, ref. 130-097-678) microbeads and the enrichment in glial populations was checked by flow cytometry (BD FACSCanto II) with Anti-ACSA-2-PE (1:100, Miltenyi, ref. 130-123-284). For dead cell removal and washing prior to single cell sequencing, Debris Removal solution (Miltenyi, ref. 130-109-398) was used. The effluent containing the live cell fraction was centrifuged at 300g for 10 min, washed and finally resuspended in 1X PBS containing 0.04% BSA in a concentration of 7 x 105 cells/ml, placing the cells on ice. Cells suspended in PBS-BSA were tested for the optimal viability and free of debris and aggregates. Cell sample was loaded onto a 10x Chromium Single Cell controller chip B (10x Genomics) as described in the manufacturer's protocol (Chromium Single Cell 3'GEM, Library & Gel Bead Kit v3, ref. PN-1000075). Intended targeted cell recovery of ~10000 cells. Generation of gel beads in emulsion (GEMs), barcoding, GEM-RT clean-up, cDNA amplification and library construction were all performed as recommended by the manufacturer. scRNA-seq libraries were sequenced with an Illumina NextSeq 550 (using v2.5 reagent kits) in paired-end fashion (28bp + 56bp bases). The bollito(56) pipeline was used to perform read analysis, as follows: Sequencing quality was checked with FastQC (http://www.bioinformatics.babraham.ac.uk/projects/fastqc/). Reads were aligned to the mouse reference genome (GRCm38, vM25 gene annotation from GENCODE(57) with STARsolo (STAR 2.7.3a) (58). Seurat 3.2.2(59) was used to check the quality of sequenced cells, explore and quantify single-cell data, obtain cell

clusters and specific gene markers. For the annotation of the different cell subtypes, signatures from Zeisel et al. 2015(60); Habib et al. 2020(61) and Batiuk, Martirosyan et al. 2020(62) were used. For astrocytes annotation, signatures in SuppTable13 were applied.

For analyzing potential interaction among clusters, we calculated the differential expressed genes for each cluster and ran a protein-protein interaction (PPI) network analysis with STRING database(63) information. Ligand-receptor interactions between cluster 3 and cluster 7 were selected and filtered based on experimental and combined scores.

In the case of human samples, for which written informed consent was obtained from all patients included in this study, Chromium Fixed RNA Profiling was used (10X Genomics). 25-50 mg of fresh biopsies were fixed in 1 ml of Fixation Buffer containing 4% Formaldehyde. After 22 hours at 4 ºC, fixed tissue was digested with a liberase-based solution using gentleMACS™ Octo Dissociator (Miltenyi, ref. 130-096-427) and the following protocol: 20 min at 37°C, 50 rpm, spin for 30 sec at 37°C, 2,000 rpm (clockwise) and spin for 30 sec at 37°C, 2,000 rpm (counter clockwise). Then, sample was kindly centrifuge and pellet was resuspended in 1ml of chilled Quenching buffer. After cell counting and for long term storage, glycerol (10 %) and Enhancer were added for cryopreservation. Fixed cell suspensions obtained with the Chromium Next GEM Single Cell Fixed RNA Sample Preparation Kit (10xGenomics PN-1000414) were processed with the Chromium Fixed RNA Profiling Reagent Kit according to the manufacturer's instructions (10xGenomics, user guide CG000527). Briefly, samples were hybridised to a human transcriptome probe set (Chromium Fixed RNA Kit, 10xGenomics PN1000474) and encapsulated in gel beads in emulsion (GEMs) in a Chromium iX instrument (10xGenomics). GEM recovery and gene expression library construction were all performed as recommended by the manufacturer. Libraries were sequenced with an Illumina NextSeq 550 (using v2.5 reagent kits) in paired-end fashion (28bp + 56bp bases). Raw images generated by the sequencer are submitted to analysis, per-cycle basecalling and quality score assignment with Illumina's Real Time Analysis integrated primary analysis software (RTA v2). Conversion of BCL (base calls) binary files to FASTQ format is subsequently performed with bcl2fastq2 (Illumina). For data analysis, cellranger-7.0.0 was used to generate the count matrices that then were subjected to QC procedures in R to discard cells with low counts across all genes. Filtered matrices were normalized by scaling normalization(64) using the Batchelor R package (https://bioconductor.org/packages/release/bioc/html/batchelor.html). Dimensionality reduction, graph-based cell clustering and cluster visualization using the Scran R package (https://bioconductor.org/packages/release/bioc/html/scran.html) were performed. Clusters were automatically annotated as described in Wang et al. (65). SingleR was used to predict the cell type using the Human Primary Cell Atlas(66) as reference. Doublet detection on clustering results was based on two approaches from the scDblFinder R package (https://bioconductor.org/packages/release/bioc/html/scDblFinder.html). The first approach detects doublets as clusters with expression profiles lying between two other clusters, and the second involves artificially stimulating doublets from the expression data and then training a classifier to identify putative doublet calls among real cells. For integration, datasets were corrected for differences in gene detection and sequencing depth. Batch effects were addressed using the Mutual Nearest Neighbors (MNN) with the fastMNN function of the batchelor package(67).

Flow cytometry

Cell suspensions were obtained from brains processed according to Korin et al. (55) or from the spleen of 10–15-week-old C57BL/6 mice. For T cells *in vitro* experiments, spleens were pressed through a 70 µm cell strainer and red blood cells were lysed with ACK Lysing Buffer (Lonza, ref. 10-548E). For intracellular stainings of CD8+ T cells *in vitro* culture, eBioscience Cell Stimulation Cocktail (plus protein transport inhibitors) (500X) were used (2 µl per ml, Invitrogen, ref. 00-4975-9). Resulting cells suspensions were incubated for 10 min with Fc Block (1:100, BD Biosciences, ref. 553141) in staining buffer (ebioscience, ref. 00-4222-26) and incubated for 30 min with the corresponding primary antibodies (SuppTable 25) in staining buffer. In the case of intracellular stainings, D Cytofix/Cytoperm™ Fixation/Permeabilization Kit (BD Biosciences, ref. 554714) was used. After washing, cells were resuspended in staining buffer and acquired either on a FACS Symphony, LSR Fortessa X20 or FACSCanto II flow cytometers (BD Biosciences) with optimised settings through voltration experiments. Cell sorting experiments were carried out on a FACSAria IIu cell sorter (BD Biosciences).

Rhapsody

For tissue dissociation, mouse brains were transferred to RPMI-1640 medium and dissociated gently using a 15-ml dounce homogenizer and then, the protocol described by Korin et al(55) was followed. Top layer of myelin was removed, cells from the interphase were collected with a Pasteur pipette and washed with Staining Buffer (PBS-/-, containing 5% FBS and 2 mM EDTA). Cells were centrifuged (10.000 G, 1 min, 4 ºC) and stained for flow cytometry. Target population (DAPI-CD45+CX3CR1-) was sorted in a FACSAria Fusion sorter (BD Biosciences) into 1.5 mL Lowbind Eppendorf tubes (Eppendorf, ref. 0030122348). In some cases, cells were separated by magnetic beads using Mouse CX3CR1 positive Selection Kit (MojoSort, ref. 480056) to remove unwanted cells, and the negative fraction was collected in Lowbind Eppendorf tubes. For scRNA-seq cell capture, library preparation, sequencing and analysis, each sample was barcoded with the Single Cell Labelling of BD™ Single-Cell Multiplexing kit following manufacturer's instructions. Single cell capture and cDNA synthesis preparation were performed following manufacturer's instructions with the BD Rhapsody™. mRNA Targeted and Sample Tag Library Preparation were prepared according to BD Rhapsody™ Targeted mRNA and AbSeq Amplification Kit protocol using BD Rhapsody™ Immune Response Panel Mm kit (ref. 633753). The concentration of PCR products and amplified libraries were determined with a Qubit fluorometer using the Qubit®dsDNA HS assay kit (Invitrogen, ref. Q32854). Their size distribution was assessed running an aliquot on an Agilent Technologies 2100 Bioanalyzer, using an Agilent High Sensitivity DNA Chip (Agilent Technologies, ref. 5067-4626). Sequencing was performed in a NovaSeq 6000 system. Library demultiplexing and targeted gene-expression library were aligned using Seven Bridges Genomics platform following the BD Biosciences Rhapsody pipeline (BD Biosciences). Cell clustering and gene expression analysis was performed using Seurat v4.1.1(68).

T cells *in vitro* culture

CD8+ T cells were obtained from the spleen of 10-15 weeks old C57BL/6 female mice. The whole organ was pressed through a 70-µm cell strainer and red blood cells were lysed with ACK Lysing Buffer (Lonza, ref. 10-548E). Cells were resuspended in HBSS 1X supplemented with 2% FBS and 1 mM EDTA at a

concentration of 108 cells/ml. EasySep™ Mouse Total CD8+ T Cell Isolation Kit (STEMCELL, ref. 19853A) protocol was followed as indicated by the manufacturer to select total CD8+ T cells. Dynabeads™ Mouse T-Activator CD3/CD28 (Thermo Scientific, ref. 11456D) were used to activate the CD8 T cells in culture. After 24 hours, the dynabeads were removed from the culture with the help of a magnetic particle concentrator. CD8+ T cells were cultured in RPMI-1640 medium supplemented with 10% FBS, 2 mM L-glutamine, 1 mM Sodium Pyruvate, 100 IU/ml penicillin/streptomycin, 50 µM ß-Mercaptoethanol,1 mM Hepes and Human IL2 (Miltenyi, ref. 130097743). When using CD8+T cells sorted from the spleen, T cells were activated with anti-mouse CD3e clone 145-2C11 (1 µg/ml, BD Biosciences, ref. 553066) coated plates, soluble anti-mouse CD28 (37.51) (1 µg/ml, Tonbo Biosciences, ref. 70-0281-U500) and mouse IL-2 (0.1 µg/ml, Miltenyi Biotec, ref. 130-094-054), in RPMI medium supplemented with 10% FBS and Penicillin-Streptomycin. CD8+ T cells were maintained in culture for one day before conditioned medium (CM) from STAT3+ and STAT3- astrospheres was added. Two to three days after addition of CM, flow cytometry was performed using the appropriated conjugated antibodies. Activated CD8+ T cells incubated with CM from astrospheres were added to B16/F10-BrM cells in a ratio 1:5 (cancer cell: CD8+ T cell) for viability assays that were analyzed by bioluminescence.
OT-I T cells extracted from the spleen of Tg(TcraTcrb)1100Mjb/J and maintained in *in vitro* culture after stimulation with 40 pM OVAlbumin-derived SIINFEKL peptide(29) were used in cytolysis assays in a ratio 1:4 (cancer cell: CD8+ T cell).
Anti-TIMP1 antibody (102D1) (10 µg/ml, Thermofisher, ref. MS608PABX) or rTIMP1 (100 ng/mL, R&D Systems, ref. 980-MT) were added at day 0 when indicated.

Phosphoproteomics

CD8+ T cells were obtained from the spleen of 10-15 weeks old C57BL/6 female mice and selected, activated and expanded as described above by using EasySep™ Mouse Total CD8+ T Cell Isolation Kit (STEMCELL, ref. 19853A). After conditioned medium (CM) from astrospheres was added, cell density was maintained at 500,000 cells/ml. Two days after addition of CM, T cells pellet was washed with PBS 1X three times and sample was prepared for proteomic analysis.
Lymphocytes were lysed 15 minutes at 95 °C in 5% SDS, 100mM Tris/HCl pH 8.0. After cooling, lysate was incubated at 25 ºC with 10 units of DNAse (Benzonase, Merk) and sonicated 10 minutes in a Bioruptor for DNA shearing. Protein concentration was determined using BSA as standard. Then, samples were digested using on bead protein aggregation capture (PAC) with MagReSyn® Hydoxyl microparticles (ratio Protein/Beads 1:5) in an automated King Fisher instrument (Thermo). Proteins were digested 16 h at 37 ºC, with 300 µl of a mixture of trypsin/LysC in 50 mM TEAB pH 8.0 (Trypzean trypsin, Sigma, LysC endoprotease, Wako, protein:enzyme ratio 1:100 each). Resulting peptides were speed-vac dried and re-dissolved in 100 µl of 200 mM HEPES pH 8.5.
Samples (approximately 100 µg) were labeled 1 h at 25 ºC using Thermo Scientific TMTpro 18plex™ Isobaric Label Reagent. Reaction was quenched/stopped by adding 5% hydroxylamine. Samples were mixed in 1:1 ratio based on total peptide amount, which was determined from an aliquot by comparing overall signal intensities on a regular LC-MS/MS run. The final mixture was finally desalted using a Sep-Pak C18 cartridge (Waters) and dried prior high pH reverse phase HPLC pre-fractionation.

Labeled peptides were pre-fractionated offline by means of high pH reverse phase chromatography using an Ultimate 3000 HPLC system equipped with a sample collector. Briefly, peptides were dissolved in 100 µL of phase A (10 mM NH4OH) and loaded onto a XBridge BEH130 C18 column (3.5 µm, 150 mm length and 1 mm ID) (Waters). Phase B was 10 mM NH4OH in 90% CH3CN. The following gradient (flow rate of 100 µL/min) was used: 0-50 min 0-25% B, 50-56 min 25-60% B, 56-57 min 60-90% B. One-minute fractions from minute 15 to 65 were collected, neutralized with 10 µl of 10% formic acid and immediately vacuum dried. Based on the UV absorbance at 280nm, 40 fractions were pooled in 8 fractions for phosphopeptide enrichment.

Phosphopeptides were enriched with MagReSyn® Zr-IMAC HP beads in an automated King Fisher instrument, using the manufacturer protocol. Eluted fractions, enriched in phosphopeptides, were immediately acidified with 10% formic acid and dry in a vacuum dryer. Flowthrough for each pool was further fractionated by micro RP-High PH in four fractions and kept for total proteome analysis.

LC-MS/MS was done by coupling an UltiMate 3000 RSLCnano LC system to an Orbitrap Exploris 480 mass spectrometer (Thermo Fisher Scientific). Samples were loaded into a trap column (Acclaim™ PepMap™ 100 C18 LC Columns 5 µm, 20 mm length) for 3 min at a flow rate of 10 µl/min in 0.1% FA. Then, peptides were transferred to an EASY-Spray PepMap RSLC C18 column (Thermo) (2 µm, 75 µm x 50 cm) operated at 45 °C and separated using a 90 min effective gradient (buffer A: 0.1% FA; buffer B: 100% ACN, 0.1% FA) at a flow rate of 250 nl/min. The gradient used was, from 4% to 6% of buffer B in 5 min, from 6% to 25% B in 70 minutes, from 25% to 45% B in 14 minutes, plus 10 additional minutes at 98% B.

The mass spectrometer was operated in a data-dependent mode, with an automatic switch between MS and MS/MS scans using a top 15 method. (Intensity threshold ≥ 5e4, dynamic exclusion of 20 sec and excluding charges unassigned, +1 and ≥ +6). MS spectra were acquired from 350 to 1500 m/z with a resolution of 60,000 FMHW (200 m/z). Ion peptides were isolated using a 0.7 Th window and fragmented using higher-energy collisional dissociation (HCD) with a normalized collision energy NCE of 36. MS/MS spectra were acquired with a fixed first mass of 120 m/z and a resolution of 45,000 FMHW (200 m/z). The ion target values were 3e6 for MS (maximum IT 25 ms) and 1e5 for MS/MS (maximum IT, auto). For data analysis, raw files were processed with MaxQuant (v 2.1.4.0) using the standard settings against a mouse protein database (UniProtKB/TrEMBL, 21,990 sequences) supplemented with contaminants. Carbamidomethylation of cysteines was set as a fixed modification whereas oxidation of methionines, protein N-term acetylation, phosphorylation of S, T, Y and N/Q de-amidation as variable modifications. Minimal peptide length was set to seven amino acids and a maximum of two tryptic missed-cleavages were allowed. Results were filtered at 0.01 FDR (peptide and protein level).

Afterwards, the phosphosite or protein intensities files were loaded in Prostar (v1.30.0) (Wieczorek et al, Bioinformatics 2017) (69) using the intensity values for further statistical analysis. Briefly, proteins/sites with less than eighteen valid values were filtered out. Then, a global normalization of log2-transformed intensities across samples was performed using the LOESS function. Differential analysis was done using the empirical Bayes statistics Limma. Proteins with a p.value < 0.05 and a log2 ratio > 0.3 or < -0.3 were defined as regulated. The FDR was estimated to be below 5% by Benjamini-Hochberg.

Sampling of human tissues

Human brain metastasis tissue, peripheral blood and cerebrospinal fluid (CSF) were collected by CNIO Biobank as backbone of a collaborative nationwide multicenter cohort, RENACER, integrated by 19 different hospitals and coordinated from CNIO Biobank. Written informed consent from each donor is collected from each patient included in this study and surplus diagnostic samples are shipped to CNIO in less than 24h from surgery, under controlled temperature and other pre-analytical variables, to warranty homogeneity and quality of the cohort. All the studies were conducted in accordance with recognized ethical guidelines (Declaration of Helsinki) and were approved by our Institutional Review Board (IRB) (CEI PI 25_2020-3). Comprehensive clinical information is also collected by CNIO Biobank associated to the samples.

Patient-derived organotypic brain cultures

Surgically-resected human brain metastases which have the advantage of including the immune tumor microenvironment from patients with lung cancer (7 cases), breast cancer (2 cases), melanoma (4 cases) or other primary sources (2 cases), were obtained from the CNIO Biobank that previously received them from Hospital Universitario 12 de Octubre, Complejo Hospitalario Universitario de Albacete, Hospital Álvaro Cunqueiro Vigo, Complejo Universitario de Navarra, Hospital Universitario de Burgos and Hospital Universitario de Bellvitge. All samples were in compliance with protocols approved by our Institutional Review Board (IRB) (CEI PI 25_2020-3). Written informed consent was signed by all patients included in this study. PDOCs were generated as described previously(70). Briefly, after neurosurgical resection, brain metastasis samples were directly collected in Neurobasal-A media (ThermoFisher Scientific, ref. 21103049) supplemented with 1 µg/ mlamphotericin B, 100 IU/ml penicillin/streptomycin, 25 ng/ml basic human fibroblast growth factor, 100 ng/ml IGF1, 25 ng/ ml EGF, 10 ng/ml neuroregulin-1 β1 (NRG1; R&D Systems, ref. 396-HB) 1× N-2 supplement (Gibco, ref. 17502048) and 1× B27 supplement. Organotypic brain cultures were prepared as described above. Slices from brain metastases were cultured in the presence of human IgG (BioXell, ref. BE0092), Anti-TIMP1 (Thermofisher, ref. MS608PABX) and Anti-CD8 (BioXcell, ref. BE0004-2) at 10 µg/µl for three days. Brain slices were fixed in 4% PFA overnight at 4 °C, and then free-floating immunofluorescence was performed. Proliferation was evaluated by manually counting Ki67+ nuclei from cancer cells.

Spheroids assays

Human samples were disaggregated mechanically, ACK Lysing Buffer (Lonza, ref. 10-548E) was used to lysis red cells and the samples were digested with DMEM supplemented with 0.125% collagenase III and 0.1% hyaluronidase at 37 ºC for 45 min. After PBS 1x washing, cells were resuspended in Neurobasal-A media supplemented as described for PDOCs, and astrospheres conditioned medium (CM) and drugs were added (Anti-TIMP1, 10µg/ml, Thermofisher, ref. MS608PABX). Spheroids were maintained in culture in low attachment plates for a maximum of three days. For immunofluorescence staining, spheroids were fixed using CytoSpin™ (Thermo Scientific) and paraformaldehyde (4%).

Clinical samples

Brain metastases from lung cancer (7 cases), breast cancer (3 cases), melanoma (11 cases) or from other primary origins (4 cases) were obtained from the CNIO

Biobank that previously received them from Hospital Universitario 12 de Octubre, Complejo Hospitalario Universitario de Albacete, Hospital Álvaro Cunqueiro Vigo, Complejo Universitario de Navarra, Hospital Universitario de Burgos and Hospital Universitario de Bellvitge. All samples were in compliance with protocols approved by our Institutional Review Board (IRB) (CEI PI 25_2020-3) and the Institutional Review Board of Department of Neuroscience, University of Turin. Written informed consent was signed by each patient include in this study. Cases were selected to include only samples with peritumoral tissue in order to evaluate the microenvironment surrounding brain metastasis. Immunohistochemistry was performed at the CNIO Histopathology Core Facility using standardized automated protocols and multiplex was performed at Institute of Immunology (Faculty of Medicine Carl Gustav Carus).

TIMP1 detection in liquid biopsies

To determine the concentration of TIMP1 in mice plasma, around 500 µL of blood were centrifuged (500 g for 10 min at 10 ºC, and the resulting supernatant fraction, again at 3,000 g for 20 min at 10 °C) immediately after the extraction. For detection of TIMP1 secreted in mice cerebrospinal fluid (CSF), CSF was extracted from the cisterna magna of anesthetized animals with a capillary tube, then it was centrifuged 600g for 5min at 4ºC. TIMP1 levels were measured using ELISA as indicated by the manufacturer (Sigma Aldrich, ref. RAB0468).

For liquid biopsies a patient cohort of 6 plasma samples from non-cancer patients were obtained from Center for Applied Clinical Research (CIMA)-Navarra University, patients with lung cancer brain metastasis (6 cases), breast cancer brain metastasis (2 cases), melanoma brain metastasis (1 case) and brain metastasis with other primary tumors (2 cases) were obtained from the CNIO Biobank that previously received them from Hospital Universitario 12 de Octubre and Hospital Álvaro Cunqueiro Vigo. CSF samples from 5 non-cancer patients were obtained from the Biobank of Hospital Universitario Virgen de la Macarena, patients with lung cancer brain metastasis (6 cases), breast cancer brain metastasis (2 cases), melanoma brain metastasis (1 case) and brain metastasis with other primary tumors (2 cases) were obtained from the CNIO Biobank that previously received them from Hospital Universitario 12 de Octubre and Hospital Álvaro Cunqueiro Vigo. All samples were in compliance with protocols approved by their respective institutional review board (IRB) (B.0001601, CEI PI 25_2020-v2 and CEI PI 25_2020-3). Written informed consent was signed by each patient included in this study. TIMP1 levels in patients' plasma and CSF were measured by ELISA following the manufacturer's instructions (Sigma Aldrich, ref. RAB0466).

Survival analysis

Survival data of 10 patients with brain metastases from different solid tumors were available. Mean (range) TIMP1 levels of the cohort (5-317 µg/ml) was used to determine high TIMP1 (>167 ng/ml) and low TIMP1 (<167 ng/ml). Kaplan Meier product limit method was generated for survival estimations. Log-rank test was performed to analyze survival differences between TIMP-1 levels in liquor (high vs. low). A two-sided p-value of <0.05 was considered to indicate statistical significance.

Immune cluster analysis

Transcriptomic data was used to cluster a total of 108 brain metastatic samples into high, medium and low immune following methodology in García-Mulero et al(26).

Gene expression of selected genes was compared between the three groups by non-parametric methods. To select biomarkers of high immune metastases, the best combination of marker genes was selected from a list of candidate genes by a binary decision tree with cross validation (k= 10) that identified the optimal classification model for high/low differentiation. R package caret was used to perform the selection. High and Low samples (n= 44) were randomly divided into Training (75%, n= 33) and Test (25%, n= 11) datasets. The Training datasets was used for classification and the Testing dataset for evaluation of the prediction accuracy. Prediction accuracy was evaluated by calculating the sensitivity, specificity, and area under the curve (AUC).

For the validation with samples from the RENACER cohort (n=135) or subcohorts with specific samples, raw reads preprocessing was performed as detailed: QuantSeq 3' mRNA-Seq reads from brain metastatic samples were processed closely following Lexogen's QuantSeq 3' mRNA-Seq Kit and integrated data analysis pipeline on Bluebee platform (015UG108V0140).FastQC (v.0.11.9) was used to generate QC reports of the sequencing reads. Raw reads were then trimmed with bbduk (bbmap v.38.93) to remove both the poly-A tail and adapter sequences. Trimmed reads were aligned with STAR v2.7.8a(58). to the GRCh38 reference with custom ENCODE settings as suggested by the aforementioned protocol and indexed with samtools v1.14(50), Finally, mapped reads were counted and aggregated to gene level counts with htseq-count v.0.13.5(51) and the Gencode v38 comprehensive gene annotation. For count normalization and batch correction, normalization and variance-stabilization of the raw counts was performed by DESeq2 v1.34.0, vst function(52). Then, we used limma v3.50.1(71) to fit a linear model of the normalized counts including both the batch and the primary site of each metastatic sample. Afterwards, the batch component was removed using removeBatchEffect, while preserving the differences associated with the primary site of the sample. For the immune cluster classification, the normalized and regressed gene expression matrix was used to assess the immune cluster profile of each sample and cluster them according to the methods of García-Mulero et al(26). For the analysis of RENACER cohort or the specified subsets of samples, single sample enrichment scores were calculated for a set of immune signatures defined by the authors using the GSVA package(72). Then, samples were grouped by agglomerative hierarchical clustering with Ward-D2 as linkage method over the euclidean distance of the enrichment scores. Finally, the resulting dendrogram was split with the R package dendextend v1.16.0 to generate three categories, each representing different immune and inflammatory profiles. All the bioinformatic analyses were carried out in R v4.1.1.

Gene set enrichment analysis

GSEAPreranked(73) was used to perform gene set enrichment analysis for the selected signature collections on a preranked gene list according to the t-statistic, setting 1000 gene set permutations. Gene sets with significant enrichment levels (FDR q-value < 0.25) were considered.

Quantification and statistics

Data was analyzed using GraphPad Prism 8 software (GraphPad Software). For comparisons between two experimental groups in datasets that followed a normal distribution, an unpaired, two-tailed Student's t-test was used. For multiple comparisons, ANOVA test was performed. For survival curves, P values were

obtained with log-rank (Mantel–Cox) two-sided tests. Chi squared test was performed for the comparison of group proportions. For CD8+CD63+ T cells qPCRs a relative scale is used for the representation that takes the minimum and maximum values for each gene.

Datasets and GEO access references

The mass spectrometry proteomics data have been deposited to the ProteomeXchange Consortium via the PRIDE partner repository with the dataset identifier PXD040436. Bulk RNAseq data from CD8+ T cells have been deposited to GEO with the dataset identifier GSE228364. scRNAseq data from experimental brain metastasis have been deposited to GEO with the dataset identifier GSE228368 and scRNAseq data from human samples have been deposited to GEO with the dataset identifier GSE254379. Rhapsody scRNAseq data data have been deposited to GEO with the dataset identifier GSE228379.

Bibliography

1. Valiente M, Ahluwalia MS, Boire A, Brastianos PK, Goldberg SB, Lee EQ, et al. The evolving landscape of brain metastasis. Trends Cancer. 2018;4:176–96.
2. Margolin K, Ernstoff MS, Hamid O, Lawrence D, McDermott D, Puzanov I, et al. Ipilimumab in patients with melanoma and brain metastases: an open-label, phase 2 trial. Lancet Oncol. 2012;13:459–65.
3. Tawbi HA, Forsyth PA, Algazi A, Hamid O, Hodi FS, Moschos SJ, et al. Combined nivolumab and ipilimumab in melanoma metastatic to the brain. N Engl J Med. 2018;379:722–30.
4. Goldberg SB, Schalper KA, Gettinger SN, Mahajan A, Herbst RS, Chiang AC, et al. Pembrolizumab for management of patients with NSCLC and brain metastases: long-term results and biomarker analysis from a non-randomised, open-label, phase 2 trial. Lancet Oncol. 2020;21:655–63.
5. Gadgeel SM, Lukas RV, Goldschmidt J, Conkling P, Park K, Cortinovis D, et al. Atezolizumab in patients with advanced non-small cell lung cancer and history of asymptomatic, treated brain metastases: Exploratory analyses of the phase III OAK study. Lung Cancer. 2019;128:105–12.
6. Long GV, Atkinson V, Lo S, Sandhu S, Guminski AD, Brown MP, et al. Combination nivolumab and ipilimumab or nivolumab alone in melanoma brain metastases: a multicentre randomised phase 2 study. Lancet Oncol. 2018;19:672–81.
7. Tawbi HA, Forsyth PA, Hodi FS, Lao CD, Moschos SJ, Hamid O, et al. Safety and efficacy of the combination of nivolumab plus ipilimumab in patients with melanoma and asymptomatic or symptomatic brain metastases (CheckMate 204). Neuro Oncol. 2021;23:1961–73.
8. Di Giacomo AM, Chiarion-Sileni V, Del Vecchio M, Ferrucci PF, Guida M, Quaglino P, et al. Primary Analysis and 4-Year Follow-Up of the Phase III NIBIT-M2 Trial in Melanoma Patients With Brain Metastases. Clin Cancer Res. 2021;27:4737–45.
9. Eguren-Santamaria I, Sanmamed MF, Goldberg SB, Kluger HM, Idoate MA, Lu BY, et al. PD-1/PD-L1 Blockers in NSCLC Brain Metastases: Challenging Paradigms and Clinical Practice. Clin Cancer Res. 2020;26:4186–97.
10. Pluim D, Ros W, van Bussel MTJ, Brandsma D, Beijnen JH, Schellens JHM. Enzyme linked immunosorbent assay for the quantification of nivolumab and

pembrolizumab in human serum and cerebrospinal fluid. J Pharm Biomed Anal. 2019;164:128–34.
11. Taggart D, Andreou T, Scott KJ, Williams J, Rippaus N, Brownlie RJ, et al. Anti-PD-1/anti-CTLA-4 efficacy in melanoma brain metastases depends on extracranial disease and augmentation of CD8+ T cell trafficking. Proc Natl Acad Sci USA. 2018;115:E1540–9.
12. Maxwell R, Luksik AS, Garzon-Muvdi T, Hung AL, Kim ES, Wu A, et al. Contrasting impact of corticosteroids on anti-PD-1 immunotherapy efficacy for tumor histologies located within or outside the central nervous system. Oncoimmunology. 2018;7:e1500108.
13. Jessurun CAC, Hulsbergen AFC, de Wit AE, Tewarie IA, Snijders TJ, Verhoeff JJC, et al. The combined use of steroids and immune checkpoint inhibitors in brain metastasis patients: a systematic review and meta-analysis. Neuro Oncol. 2021;23:1261–72.
14. Tringale KR, Reiner AS, Sehgal RR, Panageas K, Betof Warner AS, Postow MA, et al. Efficacy of immunotherapy for melanoma brain metastases in patients with concurrent corticosteroid exposure. CNS Oncol. 2023;12(1):CNS93
15. Valiente M, Obenauf AC, Jin X, Chen Q, Zhang XH-F, Lee DJ, et al. Serpins promote cancer cell survival and vascular co-option in brain metastasis. Cell. 2014;156:1002–16.
16. Priego N, Zhu L, Monteiro C, Mulders M, Wasilewski D, Bindeman W, et al. STAT3 labels a subpopulation of reactive astrocytes required for brain metastasis. Nat Med. 2018;24:1024–35.
17. Gril B, Palmieri D, Qian Y, Anwar T, Liewehr DJ, Steinberg SM, et al. Pazopanib inhibits the activation of PDGFRβ-expressing astrocytes in the brain metastatic microenvironment of breast cancer cells. Am J Pathol. 2013;182:2368–79.
18. Xing F, Kobayashi A, Okuda H, Watabe M, Pai SK, Pandey PR, et al. Reactive astrocytes promote the metastatic growth of breast cancer stem-like cells by activating Notch signalling in brain. EMBO Mol Med. 2013;5:384–96.
19. Wasilewski D, Priego N, Fustero-Torre C, Valiente M. Reactive astrocytes in brain metastasis. Front Oncol. 2017;7:298.
20. Álvaro-Espinosa L, de Pablos-Aragoneses A, Valiente M, Priego N. Brain microenvironment heterogeneity: potential value for brain tumors. Front Oncol. 2021;11:714428.
21. Kantzer CG, Boutin C, Herzig ID, Wittwer C, Reiß S, Tiveron MC, et al. Anti-ACSA-2 defines a novel monoclonal antibody for prospective isolation of living neonatal and adult astrocytes. Glia. 2017;65:990–1004.
22. Ma W, Oliveira-Nunes MC, Xu K, Kossenkov A, Reiner BC, Crist RC, et al. Type I interferon response in astrocytes promotes brain metastasis by enhancing monocytic myeloid cell recruitment. Nat Commun. 2023;14:2632.
23. Verdura S, Cuyàs E, Llorach-Parés L, Pérez-Sánchez A, Micol V, Nonell-Canals A, et al. Silibinin is a direct inhibitor of STAT3. Food Chem Toxicol. 2018;116:161–72.
24. Klemm F, Maas RR, Bowman RL, Kornete M, Soukup K, Nassiri S, et al. Interrogation of the Microenvironmental Landscape in Brain Tumors Reveals Disease-Specific Alterations of Immune Cells. Cell. 2020;181:1643–1660.e17.
25. Sutter PA, Willis CM, Menoret A, Nicaise AM, Sacino A, Sikkema AH, et al. Astrocytic TIMP-1 regulates production of Anastellin, an inhibitor of

oligodendrocyte differentiation and FTY720 responses. Proc Natl Acad Sci USA. 2024;121:e2306816121.
26. García-Mulero S, Alonso MH, Pardo J, Santos C, Sanjuan X, Salazar R, et al. Lung metastases share common immune features regardless of primary tumor origin. J Immunother Cancer. 2020;8(1):e000491
27. Valiente M, Ortega-Paino E. Updating cancer research with patient-focused networks. Trends Cancer. 2024;10:1–4.
28. Oyler-Yaniv A, Oyler-Yaniv J, Whitlock BM, Liu Z, Germain RN, Huse M, et al. A Tunable Diffusion-Consumption Mechanism of Cytokine Propagation Enables Plasticity in Cell-to-Cell Communication in the Immune System. Immunity. 2017;46:609–20.
29. Sancho D, Joffre OP, Keller AM, Rogers NC, Martínez D, Hernanz-Falcón P, et al. Identification of a dendritic cell receptor that couples sensing of necrosis to immunity. Nature. 2009;458:899–903.
30. Oelmann E, Herbst H, Zühlsdorf M, Albrecht O, Nolte A, Schmitmann C, et al. Tissue inhibitor of metalloproteinases 1 is an autocrine and paracrine survival factor, with additional immune-regulatory functions, expressed by Hodgkin/Reed-Sternberg cells. Blood. 2002;99:258–67.
31. Monteiro C, Miarka L, Perea-García M, Priego N, García-Gómez P, Álvaro-Espinosa L, et al. Stratification of radiosensitive brain metastases based on an actionable S100A9/RAGE resistance mechanism. Nat Med. 2022;28:752–65.
32. Grünwald B, Schoeps B, Krüger A. Recognizing the Molecular Multifunctionality and Interactome of TIMP-1. Trends Cell Biol. 2019;29:6–19.
33. Jung K-K, Liu X-W, Chirco R, Fridman R, Kim H-RC. Identification of CD63 as a tissue inhibitor of metalloproteinase-1 interacting cell surface protein. EMBO J. 2006;25:3934–42.
34. Warner RB, Najy AJ, Jung YS, Fridman R, Kim S, Kim H-RC. Establishment of Structure-Function Relationship of Tissue Inhibitor of Metalloproteinase-1 for Its Interaction with CD63: Implication for Cancer Therapy. Sci Rep. 2020;10:2099.
35. Justo BL, Jasiulionis MG. Characteristics of TIMP1, CD63, and β1-Integrin and the Functional Impact of Their Interaction in Cancer. Int J Mol Sci. 2021;22(17):9319
36. Pfistershammer K, Majdic O, Stöckl J, Zlabinger G, Kirchberger S, Steinberger P, et al. CD63 as an activation-linked T cell costimulatory element. J Immunol. 2004;173:6000–8.
37. Schröder J, Lüllmann-Rauch R, Himmerkus N, Pleines I, Nieswandt B, Orinska Z, et al. Deficiency of the tetraspanin CD63 associated with kidney pathology but normal lysosomal function. Mol Cell Biol. 2009;29:1083–94.
38. Ansari KI, Bhan A, Liu X, Chen MY, Jandial R. Astrocytic IGFBP2 and CHI3L1 in cerebrospinal fluid drive cortical metastasis of HER2+breast cancer. Clin Exp Metastasis. 2020;37:401–12.
39. Delgado-Peraza F, Nogueras-Ortiz CJ, Volpert O, Liu D, Goetzl EJ, Mattson MP, et al. Neuronal and astrocytic extracellular vesicle biomarkers in blood reflect brain pathology in mouse models of alzheimer's disease. Cells. 2021;10(5):993
40. Pentsova EI, Shah RH, Tang J, Boire A, You D, Briggs S, et al. Evaluating Cancer of the Central Nervous System Through Next-Generation Sequencing of Cerebrospinal Fluid. J Clin Oncol. 2016;34:2404–15.
41. De Mattos-Arruda L, Mayor R, Ng CKY, Weigelt B, Martínez-Ricarte F, Torrejon D, et al. Cerebrospinal fluid-derived circulating tumour DNA better represents

the genomic alterations of brain tumours than plasma. Nat Commun. 2015;6:8839.
42. Miller AM, Shah RH, Pentsova EI, Pourmaleki M, Briggs S, Distefano N, et al. Tracking tumour evolution in glioma through liquid biopsies of cerebrospinal fluid. Nature. 2019;565:654–8.
43. Rubio-Perez C, Planas-Rigol E, Trincado JL, Bonfill-Teixidor E, Arias A, Marchese D, et al. Immune cell profiling of the cerebrospinal fluid enables the characterization of the brain metastasis microenvironment. Nat Commun. 2021;12:1503.
44. El Rassy E, Botticella A, Kattan J, Le Péchoux C, Besse B, Hendriks L. Non-small cell lung cancer brain metastases and the immune system: From brain metastases development to treatment. Cancer Treat Rev. 2018;68:69–79.
45. Giles AJ, Hutchinson M-KND, Sonnemann HM, Jung J, Fecci PE, Ratnam NM, et al. Dexamethasone-induced immunosuppression: mechanisms and implications for immunotherapy. J Immunother Cancer. 2018;6:51.
46. Moore CS, Crocker SJ. An alternate perspective on the roles of TIMPs and MMPs in pathology. Am J Pathol. 2012;180:12–6.
47. Niesel K, Schulz M, Anthes J, Alekseeva T, Macas J, Salamero-Boix A, et al. The immune suppressive microenvironment affects efficacy of radio-immunotherapy in brain metastasis. EMBO Mol Med. 2021;13:e13412.
48. Trapnell C, Pachter L, Salzberg SL. TopHat: discovering splice junctions with RNA-Seq. Bioinformatics. 2009;25:1105–11.
49. Langmead B, Trapnell C, Pop M, Salzberg SL. Ultrafast and memory-efficient alignment of short DNA sequences to the human genome. Genome Biol. 2009;10:R25.
50. Li H, Handsaker B, Wysoker A, Fennell T, Ruan J, Homer N, et al. The Sequence Alignment/Map format and SAMtools. Bioinformatics. 2009;25:2078–9.
51. Anders S, Pyl PT, Huber W. HTSeq — a Python framework to work with high-throughput sequencing data. Bioinformatics. 2015;31:166–9.
52. Love MI, Huber W, Anders S. Moderated estimation of fold change and dispersion for RNA-seq data with DESeq2. Genome Biol. 2014;15:550.
53. Bankhead P, Loughrey MB, Fernández JA, Dombrowski Y, McArt DG, Dunne PD, et al. QuPath: Open source software for digital pathology image analysis. Sci Rep. 2017;7:16878.
54. Bayerl F, Bejarano DA, Bertacchi G, Doffin A-C, Gobbini E, Hubert M, et al. Guidelines for visualization and analysis of DC in tissues using multiparameter fluorescence microscopy imaging methods. Eur J Immunol. 2023;53(11):e2249923
55. Korin B, Dubovik T, Rolls A. Mass cytometry analysis of immune cells in the brain. Nat Protoc. 2018;13:377–91.
56. García-Jimeno L, Fustero-Torre C, Jiménez-Santos MJ, Gómez-López G, Di Domenico T, Al-Shahrour F. bollito: a flexible pipeline for comprehensive single-cell RNA-seq analyses. Bioinformatics. 2022;38:1155–6.
57. Frankish A, Diekhans M, Jungreis I, Lagarde J, Loveland JE, Mudge JM, et al. GENCODE 2021. Nucleic Acids Res. 2021;49:D916–23.
58. Dobin A, Davis CA, Schlesinger F, Drenkow J, Zaleski C, Jha S, et al. STAR: ultrafast universal RNA-seq aligner. Bioinformatics. 2013;29:15–21.
59. Stuart T, Butler A, Hoffman P, Hafemeister C, Papalexi E, Mauck WM, et al. Comprehensive Integration of Single-Cell Data. Cell. 2019;177:1888–1902.e21.

60. Zeisel A, Muñoz-Manchado AB, Codeluppi S, Lönnerberg P, La Manno G, Juréus A, et al. Brain structure. Cell types in the mouse cortex and hippocampus revealed by single-cell RNA-seq. Science. 2015;347:1138–42.
61. Habib N, McCabe C, Medina S, Varshavsky M, Kitsberg D, Dvir-Szternfeld R, et al. Disease-associated astrocytes in Alzheimer's disease and aging. Nat Neurosci. 2020;23:701–6.
62. Batiuk MY, Martirosyan A, Wahis J, de Vin F, Marneffe C, Kusserow C, et al. Identification of region-specific astrocyte subtypes at single cell resolution. Nat Commun. 2020;11:1220.
63. Szklarczyk D, Franceschini A, Wyder S, Forslund K, Heller D, Huerta-Cepas J, et al. STRING v10: protein-protein interaction networks, integrated over the tree of life. Nucleic Acids Res. 2015;43:D447-52.
64. Lun ATL, McCarthy DJ, Marioni JC. A step-by-step workflow for low-level analysis of single-cell RNA-seq data with Bioconductor. [version 2; peer review: 3 approved, 2 approved with reservations]. F1000Res. 2016;5:2122.
65. Wang Z, Wang Y, Chang M, Wang Y, Liu P, Wu J, et al. Single-cell transcriptomic analyses provide insights into the cellular origins and drivers of brain metastasis from lung adenocarcinoma. Neuro Oncol. 2023;25:1262–74.
66. Mabbott NA, Baillie JK, Brown H, Freeman TC, Hume DA. An expression atlas of human primary cells: inference of gene function from coexpression networks. BMC Genomics. 2013;14:632.
67. Haghverdi L, Lun ATL, Morgan MD, Marioni JC. Batch effects in single-cell RNA-sequencing data are corrected by matching mutual nearest neighbors. Nat Biotechnol. 2018;36:421–7.
68. Hao Y, Hao S, Andersen-Nissen E, Mauck WM, Zheng S, Butler A, et al. Integrated analysis of multimodal single-cell data. Cell. 2021;184:3573–3587.e29.
69. Wieczorek S, Combes F, Lazar C, Giai Gianetto Q, Gatto L, Dorffer A, et al. DAPAR & ProStaR: software to perform statistical analyses in quantitative discovery proteomics. Bioinformatics. 2017;33:135–6.
70. Zhu L, Retana D, García-Gómez P, Álvaro-Espinosa L, Priego N, Masmudi-Martín M, et al. A clinically compatible drug-screening platform based on organotypic cultures identifies vulnerabilities to prevent and treat brain metastasis. EMBO Mol Med. 2022;14:e14552.
71. Ritchie ME, Phipson B, Wu D, Hu Y, Law CW, Shi W, et al. limma powers differential expression analyses for RNA-sequencing and microarray studies. Nucleic Acids Res. 2015;43:e47.
72. Hänzelmann S, Castelo R, Guinney J. GSVA: gene set variation analysis for microarray and RNA-seq data. BMC Bioinformatics. 2013;14:7.
73. Subramanian A, Tamayo P, Mootha VK, Mukherjee S, Ebert BL, Gillette MA, et al. Gene set enrichment analysis: a knowledge-based approach for interpreting genome-wide expression profiles. Proc Natl Acad Sci USA. 2005;102:15545–50.

Figure legends

Figure 1. Clusters of brain metastasis-associated reactive astrocytes suggest functional diversity including immune-modulation.

A. Schema of the experimental design. Three different brains from C57BL/6J mice intracranially injected with B16/F10-BrM cells were enzymatically digested and

pooled. ACSA-2 labeling was used to enrich the sample in glial cells, obtaining 7762 cells identified as astrocytes. A pool of three brains without tumor were used as control for comparisons. **B.** Uniform manifold approximation and projection (UMAP) plot (0.2 resolution) of the different subpopulations of reactive astrocytes in brain metastasis. Dotted lines surround *Stat3*+ clusters. **C.** *Stat3* expression in the different clusters of brain metastasis-associated astrocytes. Dot size represents the dimension of the subpopulation compared to total cells and a colored scale indicates the level of expression: blue, low expression and red, high expression. **D-E.** Representation of the top upregulated GSEA pathways in Stat3+ astrocytic clusters of brain metastasis according to the normalized enrichment score (NES) and a cutoff of P value < 0.05 and FDR < 0.25. ECM, extracellular matrix. Colored pathways according to the biological category the gene sets belong to, correspond to more than half of the total pathways analyzed (total percentage of 100%). Detailed information of the pathways in SuppTable4. **F.** Schema of the experimental design. Two human brain metastases from a lung cancer and a breast cancer patients were fixed, digested and profiled for single-cell RNA-sequencing (scRNA-seq), 2612 astrocytes and 1338 astrocytes were identified, respectively. **G.** Uniform manifold approximation and projection (UMAP) plot (k= 20) of the different subpopulations of reactive astrocytes in human brain metastasis. Dotted lines surround clusters with *STAT3* high expression. **H.** *STAT3* expression in the different clusters of brain metastasis-associated astrocytes. Dot size represents the dimension of the subpopulation compared to total cells and a colored scale indicates the level of expression: blue, low expression and red, high expression. **I**. Normalized enrichment score (NES) of GSEA pathways comparing cluster 3, 4 and 5 of human brain metastases-associated astrocytes. KEGG_Cytokine-cytokine receptor interaction, p.adjust=1,05E-05; Reactome_Extracellular matrix (ECM) organization, p.adjust=1,03E-03; Reactome_Signaling by Interleukins, p.adjust=8,65E-03; Reactome_Antigen processing: Ubiquitination & Proteasome degradation, p.adjust=1,67E-02; Reactome_Cell Cycle Checkpoints, p.adjust=3,43E-03; Hallmark_Epithelial_mesenchymal_transition (EMT), p.adjust=5E-09; KEGG_ECM-receptor interaction, p.adjust=7.08E-05; HALLMARK_Interferon_alpha response, p.adjust=1.11E-02; KEGG_Proteasome, p.adjust=6.53E-04; HALLMARK_Myc Targets V1, p.adjust=2.88E-07.

Figure 2. The pro-tumoral role of STAT3+ reactive astrocytes involves immune-modulation.

A. Schema of the experimental design. Green cells: pSTAT3- astrocytes; red cells: pSTAT3+ astrocytes. Pre-activated CD8+ lymphocytes incubated with conditioned medium (CM) generated by pSTAT3- and pSTAT3+ astrospheres (as described in material and methods section) were processed for bulk RNA-sequencing. **B.** GSEA of Biological Process (GOBP) of T cell activation downregulated in T cells incubated with pSTAT3+ astrospheres CM compared to pSTAT3- astrospheres CM. n= 3 independent T cells *in vitro* cultures per condition. **C.** Schema of the experimental design. C57BL/6J mice were intracranially injected with B16/F10-BrM cells, control brains and brains from mice treated during six days with the STAT3 inhibitor, silibinin (Legasil® daily 200 mg/kg daily) were processed to obtain the immune infiltrate fraction, which was depleted from monocytes. Rhapsody system was used to single cell sequence a total of 3055 immune cells identifying different CD3+ T cells clusters**.** **D.** Quantification showing the percentage of cytotoxic-like T cells (clusters 4, 7 and 13) (FigS2C-E) in the brain of control and silibinin treated mice. Values are shown in

box-and-whisker plots, where each dot is a mouse and the line in the box corresponds to the median. The boxes go from the upper to the lower quartiles, and the whiskers go from the minimum to the maximum value (n = 8, control mice; n = 9, mice treated with silibinin). P value was calculated using two-tailed t-test between control and silibinin experimental groups. **E.** Schema of the experimental design. Tmx-treated and untreated cKO^{GFAP}-*Stat3* mice intracranially injected with B16/F10-BrM cells were sacrificed at experimental endpoint, their brains were processed to obtain the immune fraction for flow cytometry analysis or sorted for CD3+CD8+ lymphocytes for RNA isolation and qRT-PCR analysis of gene expression. **F.** Representative flow cytometry analysis of Granzyme b expression in CD3+CD8+T cells from control and cKO^{GFAP}-Stat3 brains intracranially injected with B16/F10-BrM cells. **G.** Quantification of the experiment in F. Error bars, s.e.m. Every dot is a different animal (n= 8). The P value was calculated using the two-tailed t-test. **H.** Schema of the experimental design. Brains from untreated or Tmx-treated cKO^{GFAP}-*Stat3* with IgG2 or anti-CD8 (10 mg/kg, every two days starting at day 3 post-inoculation of cancer cells) two weeks after being inoculated with B16/F10-BrM cells intracardially, were analyzed. **I.** Representative images of *ex vivo* brains in H. Images show the BLI intensity. **J.** Quantification of *ex vivo* bioluminescence (BLI). Values are shown in box-and-whisker plots where every dot represents a different animal. Values were obtained from normalizing the *ex vivo* brain signal to the *in vivo* head signal three days after intracardiac injection when treatment was initiated (n = 39/28/28 mice per experimental condition, 8 independent experiments). The P value was calculated using the two-tailed t-test.

Figure 3. TIMP1 and STAT3 in reactive astrocytes correlate with a high immune cluster classifier in human brain metastases.

A. Representative images showing pSTAT3+ TIMP1+ reactive astrocytes (arrows) in different samples: astrospheres enriched in STAT3, established brain metastasis induced by intracardiac inoculation of B16/F10-BrM cells and human breast cancer brain metastasis. Dotted line surrounds the cancer cells (cc). Scale bar, 20 μm. **B.** Schema of the experimental design. Sequencing data from patients' samples with brain metastases were stratified into low, medium and high immune categories or clusters. Immune clusters were calculated according to an initial algorithm and then complemented with a three gene classifier representing key cell types of the microenvironment. **C-D.** *STAT3* (C) and *TIMP1* (D) expression in human samples from low, medium and high immune clusters. Values are shown in box-and-whisker plots, where each dot is a patient and the line in the box corresponds to the median. The boxes go from the upper to the lower quartiles, and the whiskers go from the minimum to the maximum value (n = 32 samples, low; n= 64 samples, medium; n= 12 samples, high). The P value was calculated using the two-tailed t-test. One way ANOVA is shown to compare the three immune categories. **E.** Schema of the experimental design. A cohort of 12 human samples with extended resection including peritumoral microenvironment was used to validate sequencing data with immunohistochemistry (IHC) profile. In the IHC image STAT3+ reactive astrocytes are shown. RA: reactive astrocytes, cc: cancer cells. Scale bar, 40 μm. **F.** Multiplex representative images of low/ medium/ high immune clusters in the cohort of human samples in E. STAT3 staining and *TIMP1* RNAscope were performed in consecutive sections and allocated on the specific patient categories. n= 4 samples in low immune cluster, n= 4 samples in medium immune cluster, n= 4 samples in high immune cluster. Scale bar, 50 μm, magnification 15 μm. **G.** Graph showing the

correlation between the percentage of immune cells as quantified by multiplex and the percentage of *TIMP1*+ events per cell in the microenvironment of 12 brain metastasis samples. Dots are colored according to the immune cluster calculated for the cohort of samples: low (green)/ medium (grey)/ high (red) immune clusters. The P value was calculated using the two-tailed t-test. **H.** A representative image of a patient with melanoma brain metastasis treated with immune checkpoint blockade showing pSTAT3+ reactive astrocytes surrounding the brain metastasis lesion next to CD8+ T cells. The patient showed extracranial response, but failed to respond to ICB intracranially. The dotted line surrounds the cancer cells (cc). Scale bar, 15 µm. **I.** Representative image of multiplex in a sample of a patient in H. Magnification showing CD8+ Granzyme b+ T cells (yellow arrows) and CD8+ Granzyme b- T cells (pink arrows). Scale bar, 20 µm. **J.** Quantification of experiment in I. The graph represents the number of pSTAT3+ reactive astrocytes surrounding a CD8+ T cell with or without Granzyme b positivity in a ratio of 100 µm. A total of 40 CD8+T cells from 5 different patients where GRZ+CD8+ T cells could be identified belonging to the cohort in H were quantified. Error bars, s.e.m. Every dot is a different CD8+ T cell. The P value was calculated using the two-tailed t-test.

Figure 4. TIMP1 mediates brain metastasis in a CD8+ T cell-dependent manner. **A.** Schema of the experimental design. pSTAT3- and pSTAT3+ *wt* and pSTAT3+ cKO^{GFAP}-*Timp1* conditioned medium (with or without rTIMP1 100 ng/mL or control IgG/Anti-TIMP1 10 µg/ml) was added to CD8+ T cells and cultured with BrM cells in a 1:4 ratio (BrM-OVA cancer cells: OT-I T cells specific for the OVA-derived SIINFEKL peptide) or a 1:5 ratio (BrM cancer cells: CD8+ T cells previously activated). **B.** Quantification of the bioluminescence (BLI) signal from the experiment shown in A and representative images of B16/F10-BrM-OVA derived BLI at the initial time point and 24 hours after adding CD8+ lymphocytes pre-incubated with CM. Light orange condition refers to co-culture of OT-I T cells with B16/F10-BrM no OVA (control for antigen-specific killing). Values correspond to 24 hours BLI normalized to BLI before adding CD8+ T cells expressed in percentage respect to the mean of control experimental condition (BrM cells). Error bars, s.e.m. n =3 different co-cultures per condition. The P value was calculated using the two-tailed t-test. **C-D.** Schema of the experimental design. Control IgG or Anti-TIMP1 (10 µg/ml) were added to the medium in organotypic cultures of mouse brain with B16/F10-BrM established lesions (C) and Patient-Derived-Organotypic-Cultures (PDOC) that include the brain metastasis-associated microenvironment (D). **E.** Quantification of the BLI signal emitted by B16/F10-BrM cells in each brain slice normalized by the initial value obtained at day 0, before the addition of control IgG, Anti-TIMP1 (10 µg/ml) or Anti-CD8 (100 µg/ml). Values are shown in box-and-whisker plots where every dot represents a different organotypic culture and the line in the box corresponds to the median. Whiskers go from the minimum to the maximum value (n = 42 IgG, 39 Anti-TIMP1 and 27 Anti-TIMP1 plus Anti-CD8 independent organotypic cultures). Quantification is accompanied by representative images of wells containing brain organotypic cultures with established B16/F10-BrM metastases grown *ex vivo* for three days. The image shows the BLI intensity in each condition for each brain slice. P values were calculated using the two-tailed t-test. **F.** Quantification of the number of Ki67+ cancer cells found in IgG2 and Anti-TIMP1-treated PDOCs. Values are shown in box-and-whisker plots where every dot represents a patient and each patient is an independent experiment (n= 11). The pie chart shows all BrM-PDOCs quantified in the graph and classified according to the

specific primary tumor. P value was calculated using two-tailed t-test. **G.** Quantification of the number of Ki67+ cancer cells found in IgG2, Anti-TIMP1 (10 µg/ml) and Anti-TIMP1 (10 µg/ml) plus Anti-CD8 (10 µg/ml) PDOCs. Values are shown in box-and-whisker plots where every dot represents a patient and each patient is an independent experiment (n= 7). P value was calculated using two-tailed t-test. **H.** Schema of the experimental design. cKO^{GFAP}-*Timp1* mice were inoculated with BrM cells intracardially and after two weeks *ex vivo* brain BLI was analyzed. **I-J.** Representative images of brains from control and cKO^{GFAP}-*Timp1* mice intracardially injected with B16/F10-BrM (I) or E0771-BrM (J) cells. The image shows the BLI intensity in each condition. **K-L.** Quantification of *ex vivo* brain BLI. Values are shown in box-and-whisker plots where every dot represents a different animal. Values were obtained from normalizing the *ex vivo* brain signal to the *in vivo* head signal three days after intracardiac injection with either B16/F10-BrM (K) or E0771-BrM (L) cells (n = 26/29 mice 4 independent experiments in K and n = 28/25 mice 3 independent experiments in L). The P value was calculated using the two-tailed t-test. **M.** Representative images of CD8+ T cells in metastatic lesions growing in brains from control or cKO^{GFAP}-*Timp1* mice intracardially injected with E0771-BrM at experimental endpoint. White arrows indicate CD8+ T cells and red arrow indicate Ki67+CD8+ T cells. Scale bar, 25 µm, magnification 5 µm. **N.** Quantification of the total number of CD8+ T cells in control and cKO^{GFAP}-*Timp1* mice intracardially injected with E0771-BrM at human endpoint. Values are shown in box-and-whisker plots where every dot represents a different animal. Ten brains were analyzed in each condition. The P value was calculated using the two-tailed t-test.

Figure 5. Characterization of the influence of TIMP1 in CD8+ T cells.
A. Schema of the experimental design. pSTAT3- and pSTAT3+ *wt* and pSTAT3+ cKO^{GFAP}-*Timp1* conditioned medium (CM) was added to CD8+ T cells and flow cytometry analysis was performed. **B.** Representative flow cytometry analysis using pre-activated CD8+ T cells incubated with conditioned medium (CM) generated by pSTAT3- and pSTAT3+ *wt* or pSTAT3+ cKO^{GFAP}-*Timp1* astrospheres. **C.** Quantification of CD25 geometric mean fluorescence intensity (gMFI) in effector CD8+ T cells from A. Error bars, s.e.m. n =3 different T cells cultures per condition. The P value was calculated using the two-tailed t-test. **D-E.** Flow cytometry analysis showing the % of IFN-γ+TNFα+ (D) and exhausted PD1+LAG3+TIM3+CD39+ (E) CD8+ T cells incubated with conditioned medium (CM) generated by pSTAT3- and pSTAT3+ *wt* or pSTAT3+ cKO^{GFAP}-*Timp1* astrospheres. Error bars, s.e.m. n =3 different T cells cultures per condition. The P value was calculated using the two-tailed t-test. **F.** Schema of the experimental design. CD8+ lymphocytes from *wt* and cKO^{GFAP}-*Timp1* brains intracranially injected with B16/F10-BrM cells were analyzed by flow cytometry. **G**, **H.** Representative flow cytometry analysis of CD44 (G) and quantification of the experiment (H). Error bars, s.e.m. Every dot is a different animal (n= 5 *wt* brains and n= 5 cKO^{GFAP}-*Timp1* brains). The P value was calculated using the two-tailed t-test. **I**, **J.** Representative flow cytometry analysis of TNFα (I) and quantification of the experiment (J). Error bars, s.e.m. Every dot is a different animal (n= 8 wt brains and n= 9 cKO^{GFAP}-*Timp1* brains). The P value was calculated using the two-tailed t-test. **K**, **L**. Representative flow cytometry analysis of CD39 and PD1 (K) and quantification of the experiment (L). Error bars, s.e.m. Every dot is a different animal (n= 8 wt brains and n= 9 cKO^{GFAP}-*Timp1* brains). The P value was calculated using the two-tailed t-test.

Figure 6. TIMP1 modulates CD8+ T cells through CD63.
A. Schema of the experimental design. CD63 expression was analyzed by flow cytometry gating on CD8+ T cells from metastasis free and brains intracranially injected with B16/F10-BrM cells. **B**. Flow cytometry analysis of CD63 expression gated on CD8+T cells from brains without tumor and brains intracranially injected with B16/F10-BrM cells. Error bars, s.e.m. Every dot is a different animal (n= 3 metastasis free brains and n= 6 B16/F10-BrM brain metastases). The P value was calculated using the two-tailed t-test. **C.** Immunofluorescence of established B16/F10-BrM metastasis. CD63 is expressed on CD8+ T cells surrounding the lesion. Red arrow indicates a CD63+CD8+ T cell. Scale bar, 10 μm. **D.** Representative image showing colocalization of metastasis-associated CD8 and CD63 staining in a lung cancer brain metastasis patient. White arrow indicates a CD8+ T cell and red arrow indicates a double CD63+CD8+ T cell. Scale bar, 10 μm. **E.** Immunoblotting using Anti-TIMP1, Anti-CD63 and Vinculin antibodies showing secreted TIMP1 and CD63 binding on CD8+ T cells when co-cultured with pSTAT3+ astrospheres. Cell lysates (first line) were immunoprecipitated with IgG isotype as control (second line) and Anti-CD63 (third line). **F.** Proximity ligation assay performed on a melanoma brain metastasis sample showing TIMP1 and CD63 in close molecular proximity on CD8+ T cells. Magnification showing red dots of TIMP1-CD63 interaction (white arrows) on a CD8+ T cell highlighted with a red arrow in the main picture. Scale bar, 10 μm. **G**. Schema of the experimental design. *Wt* or CD63-null CD8+ T cells were used in *ex vivo* organotypic cultures with established B16/F10-BrM metastasis. **H.** Quantification of the BLI signal emitted by B16/F10-BrM cells in each brain slice normalized by the initial value obtained at time 0, before the addition of *wt* or CD63-null CD8+ T cells. Values are shown in box-and-whisker plots where every dot represents a different organotypic culture and the line in the box corresponds to the median. Whiskers go from the minimum to the maximum value (n = 8 no CD8+ T cells, 7 *wt* CD8+ T cells and 10 CD63-null CD8+ T cells independent organotypic cultures). Quantification is accompanied by representative images of wells containing brain organotypic cultures with established B16/F10-BrM metastases grown *ex vivo* for 24 hours. The image shows the BLI intensity in each condition for each brain slice. P values were calculated using the two-tailed t-test. **I**. Heatmap generated with the qRT-PCR analysis performed on $CD63^{high}$CD8+ T cells sorted from *wt* and cKO^{GFAP}-*Timp1* mice ten days after intracranial injection of B16/F10-BrM cells. n= 12 brains per condition and 6 brains for control condition (not injected with BrM cells). **J.** Schema of the experimental design. CD8+ lymphocytes were cultured with STAT3- astrospheres CM and *wt* or cKO^{GFAP}-*Timp1* STAT3+ astrospheres CM and processed for phosphoproteomic analysis. **K.** Heatmap showing the top 10 enriched sequence motifs found in CD8+ T cells in the absence of TIMP1 from the CM of STAT3+ astrospheres. Clustering enrichment using Fisher Exact Test was performed. P val < 0.01 FDR < 2%. **L.** Quantification of the number of pERK+CD8+ T cells in control and cKO^{GFAP}-*Timp1* mice intracardially injected with E0771-BrM at endpoint. Error bars, s.e.m. Every dot is a different animal (n= 3 brains per condition). **M.** Quantification of the number of pERK+CD8+ T cells in human brain metastases samples scored with multiplex. Violin plots show the median of % pERK+CD8+ T cells among the total CD8+ T cells per field of view (n=5-10/patient) from 3 patients analyzed in each condition. The P value was calculated using the two-tailed t-test**.** **N.** Model summarizing main findings regarding the immunomodulatory role of TIMP1 derived from STAT3+ reactive astrocytes in brain metastasis. Secreted TIMP1 acts on its receptor CD63 receptor on the surface of

CD8+ lymphocytes, modulating ERK mediated-signaling and downregulating activation of T cell markers and cytolytic enzymes and upregulating exhaustion markers, thus affecting effective T cell-mediated killing of brain metastatic cells.

Figure 7. A combined immunotherapy targeting local immunosuppression provides superior control of brain metastasis.

A. Schema of the experimental design. C57BL/6J mice were intracardially injected with B16/F10-BrM cells, after three days the following treatments were administrated: IgG2 (10 mg/kg), silibinin daily (200 mg/kg) or immune checkpoint blockade (ICB) every two days (Anti-PD1,10 mg/kg, plus Anti-CTLA4, 10 mg/kg) alone or in combination with silibinin. After two weeks, *ex vivo* analysis and histological analysis of different organs were performed. **B.** Representative images of control, ICB, silibinin and ICB plus silibinin treated mice two weeks (endpoint) after intracardiac inoculation of B16/F10-BrM cells. In *in vivo* images, dotted lines surround brain and lungs, showed in the *ex vivo* representative images below. Images show the bioluminescence (BLI) intensity. **C.** Distribution of lesions according to size (small: <5e4 μm^2, medium: 2.5e4 μm^2-2e5 μm^2, big: >2e5 μm^2). Values are represented as percentage respect to total number of lesions per each experimental condition. n= 4-6 brains per condition. P values of the different comparison calculated using the two-tailed t-test are shown in SuppTable16. **D.** Representative images of Perforin and Granzyme b staining in endpoint brains from mice treated with ICB and ICB plus silibinin. Arrows indicate positive staining. Scale bar, 50 μm. **E.** Quantification showing the number of cells expressing cytotoxic markers in D. Values are shown in box-and-whisker plots where every dot is a different lesion (n= 6 lesions in 3 brains are quantified in ICB and n=4 lesions in 3 brains are quantified in ICB plus silibinin). The P value was calculated using the two-tailed t-test. **F.** Schema of the experimental design. Three days after intracranial inoculation of B16/F10-BrM cells, 5 doses of 3Gy WBRT and IgG2 (10 mg/kg), silibinin daily (200 mg/kg) or immune checkpoint blockade (ICB) every two days (Anti-PD1,10 mg/kg, plus Anti-CTLA4, 10 mg/kg) alone or in combination with silibinin were administrated. **G.** Kaplan-Meier curve showing survival proportions of mice without radiotherapy (dotted gray line, n= 12) and with radiotherapy (Rx) (IgG2 red line, n= 8; ICB blue line, n=8, silibinin gray line, n= 8, ICB+silibinin green line, n= 8). P value was calculated using log-rank (Mantel-Cox) test between Rx and Rx+ICB+silibinin groups. **H.** Representative images of cleaved-caspase 3 staining of intracranially inoculated brains with B16/F10-BrM cells at endpoint from irradiated mice treated with ICB and ICB plus silibinin. Scale bar, 75 μm, magnification 25 μm. **I.** Quantification of experiment in H. Percentage of cleaved-caspase 3 is normalized with tumor area. Values are shown in box-and-whisker plots where every dot is a different field of view. Four brains per condition are quantified. The P value was calculated using the two-tailed t-test. **J.** Representative images of Ki67- (white arrows) and Ki67+ (red arrows) CD8+ T cells infiltrating brain metastases from mice intracranially inoculated with B16/F10-BrM cells and treated with radiotherapy and either ICB or ICB plus silibinin. Scale bar, 25 μm. **K.** Quantification of experiment in J. Values are shown in box-and-whisker plots where every dot is a different field of view. Three brains per condition are quantified. The P value was calculated using the two-tailed t-test. **L.** Quantification of TIMP1 levels measured in patients´ cerebrospinal fluid (CSF). Non-cancer control condition: n= 6 and brain metastasis condition: n= 12 (matched CSF samples from the same patients in FigS9A) plus n=2 unmatched CSF values. Each dot is a different patient. Patients shown in N are

colored in green. The P value was calculated using the two-tailed t-test. **M-N.** Schema of the strategy to perform an *ex vivo* proof of concept validation of TIMP1 as a biomarker of response to blockade of CD8+ T cell local immunosuppression. Heatmap showing immune cluster category (according to total percentage of immune cells, mean percentage of immune cells present in low immune cluster samples in Fig3G is used as reference), TIMP1 levels in the CSF (mean of TIMP1 levels in the CSF of non-cancer patients is used as reference) and response to Anti-TIMP1 and Anti-TIMP1+Anti-CD8 (viability of cancer cells in percentage of $Ki67^+$ cancer cells, IgG2 condition is used as reference) in PDOCs of patients in Fig7L (green dots). Results from the PDOCs are in Fig4F-G and SuppTable15. Represented values are shown in FigS9C.

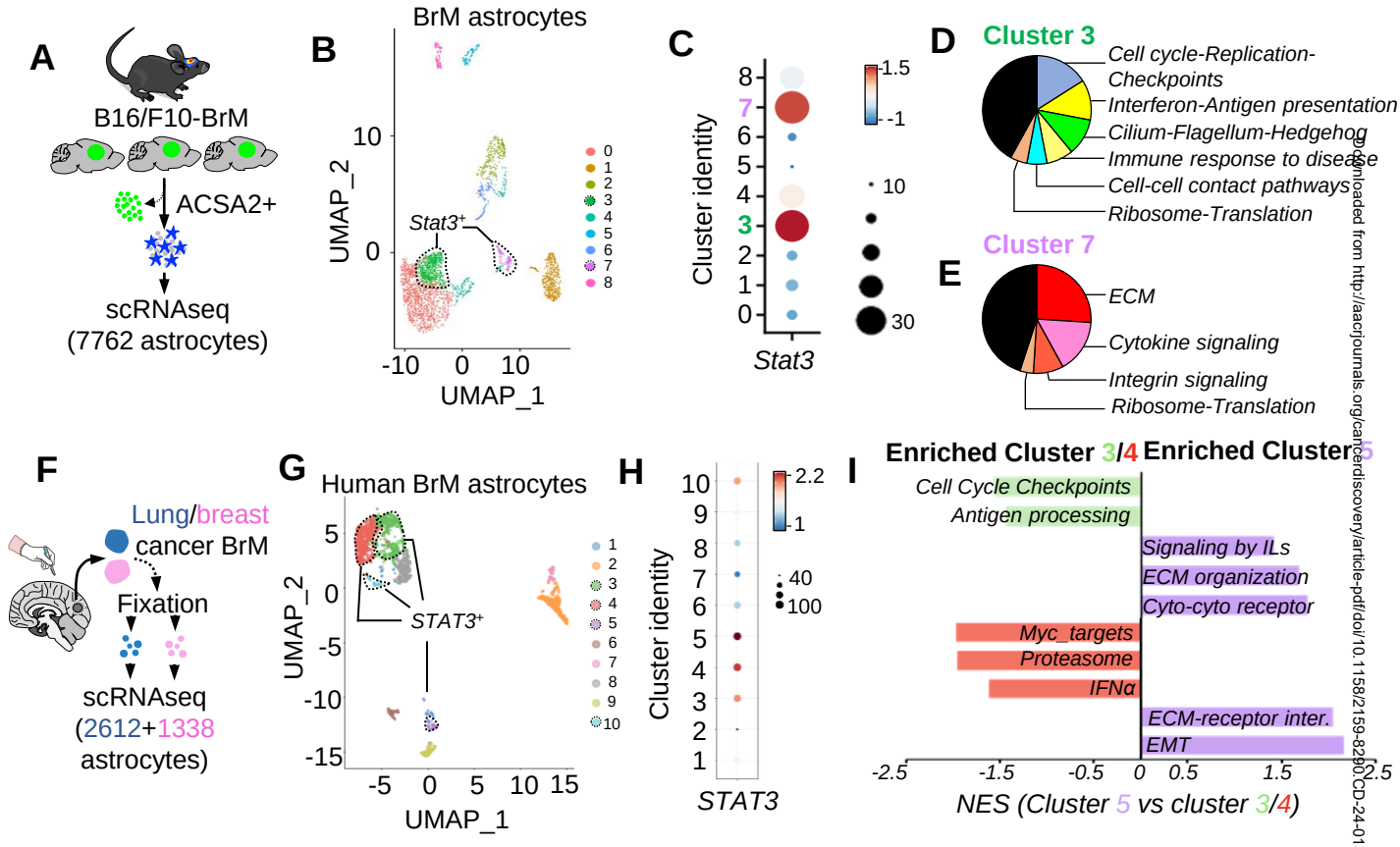

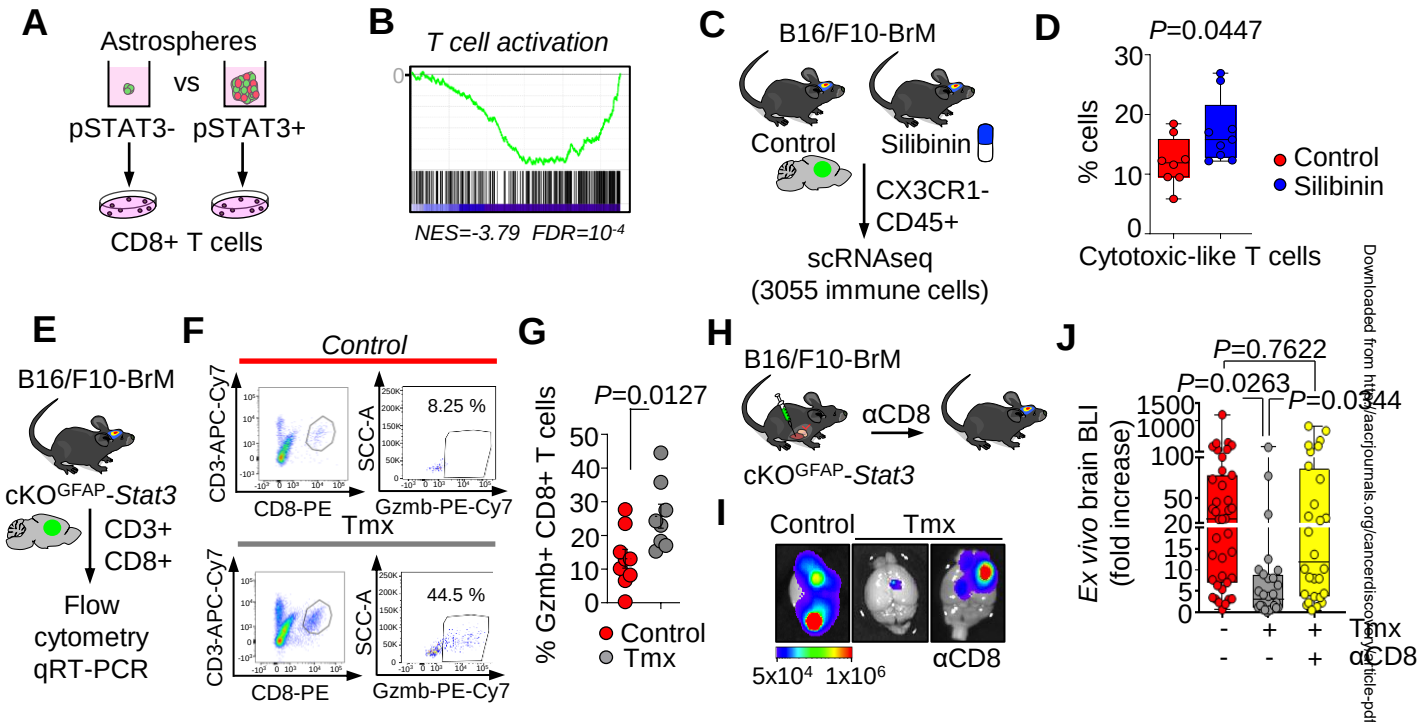

Figure 2

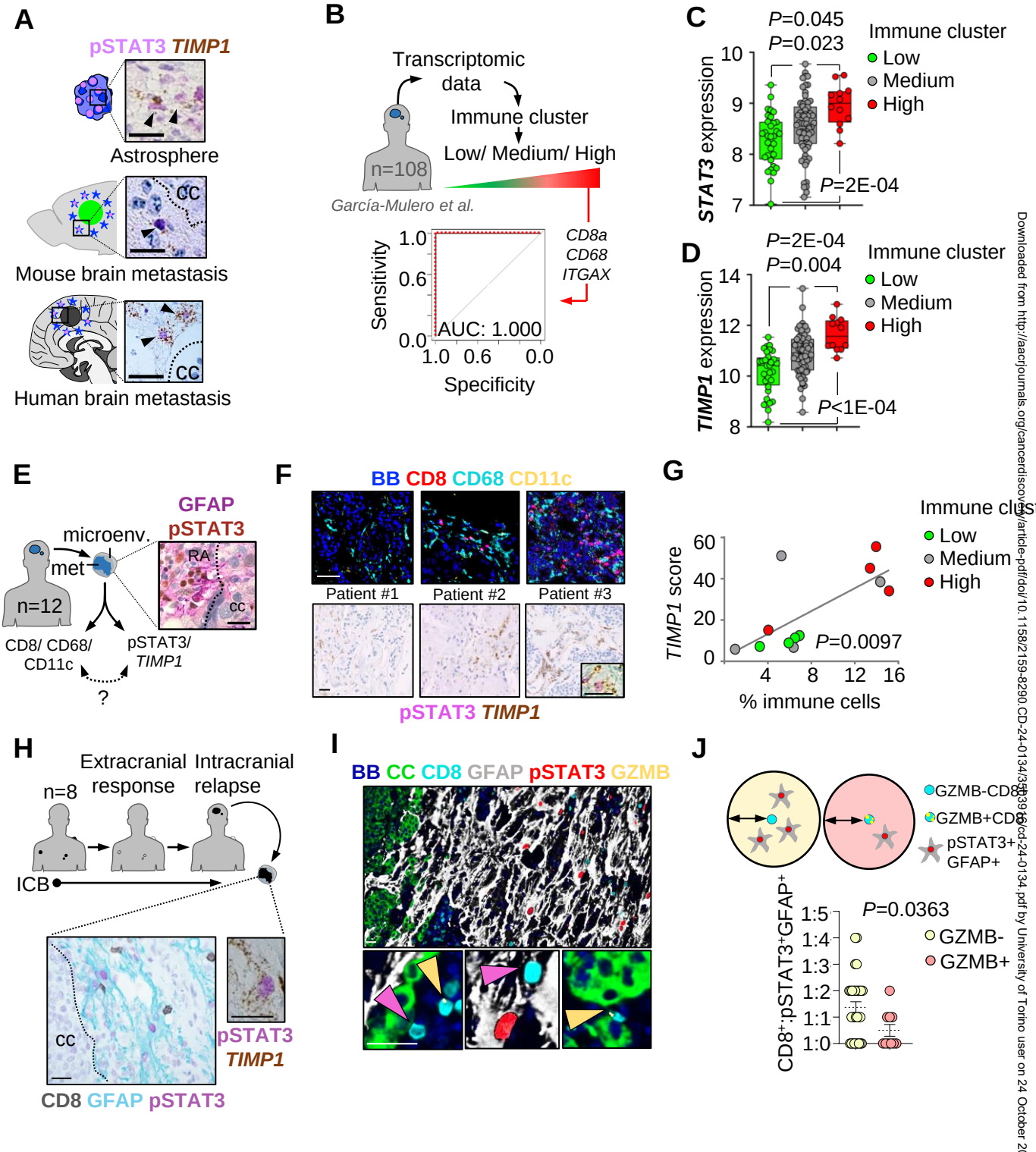

Figure 3

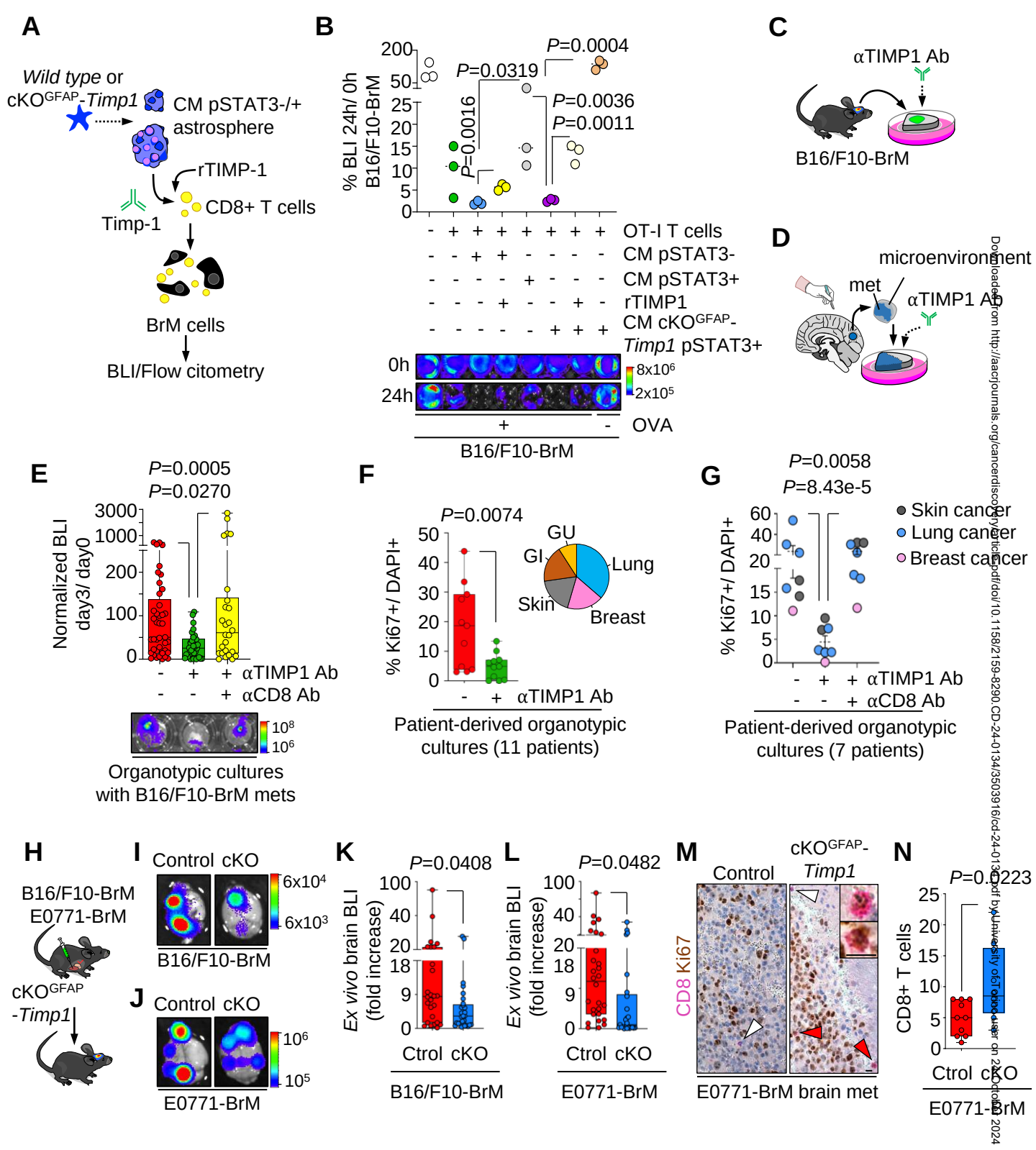

Figure 4

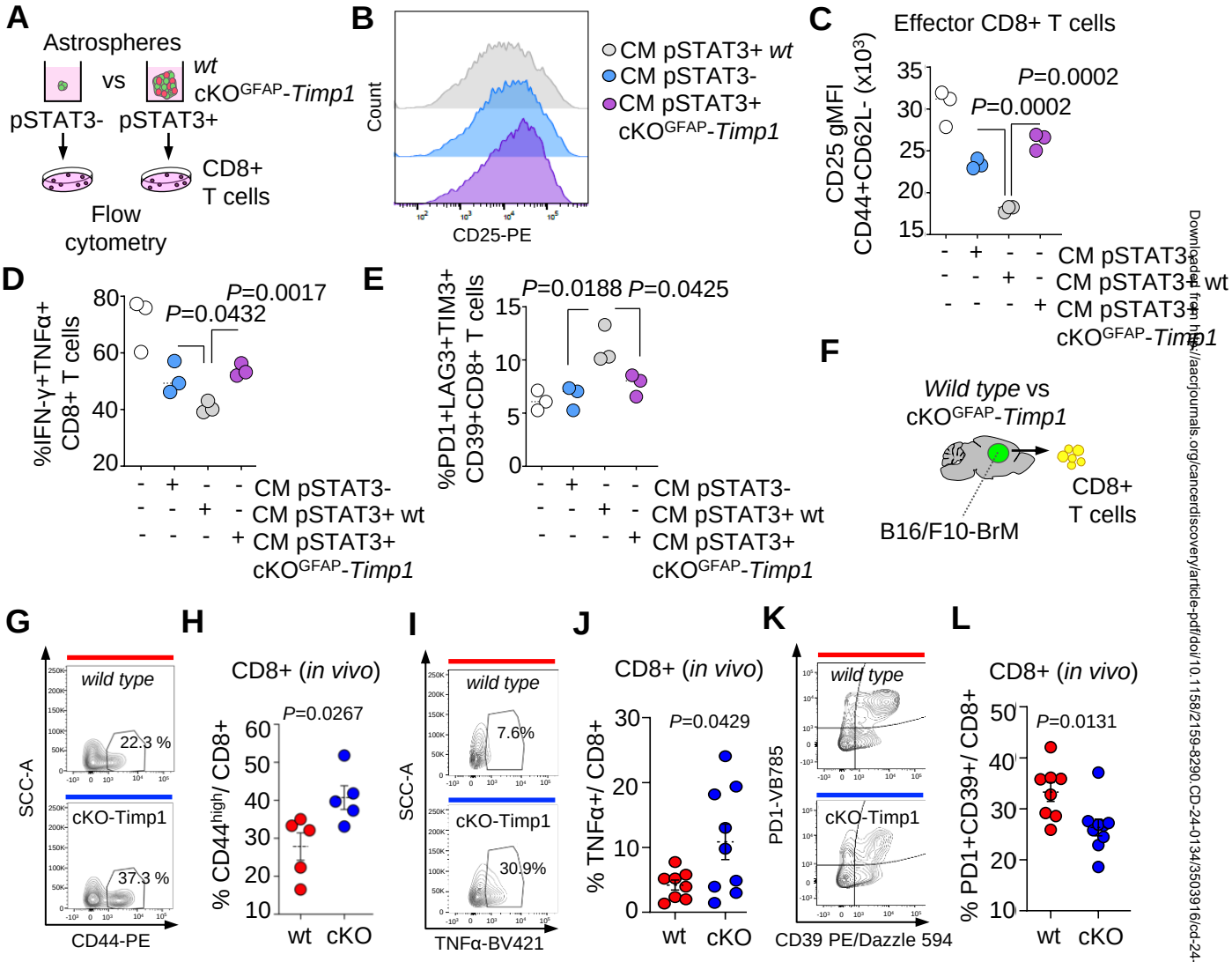

Figure 5

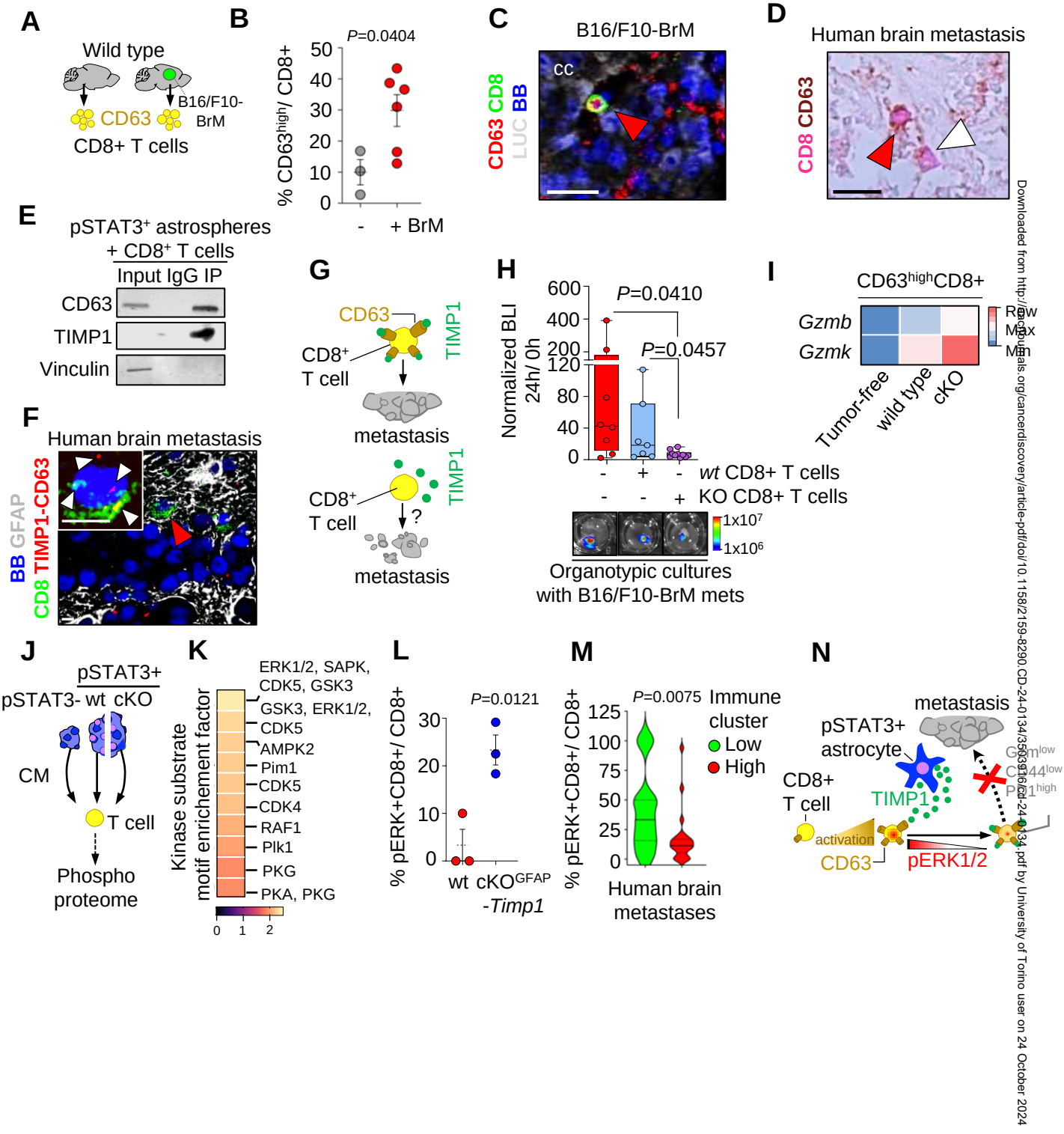

Figure 6

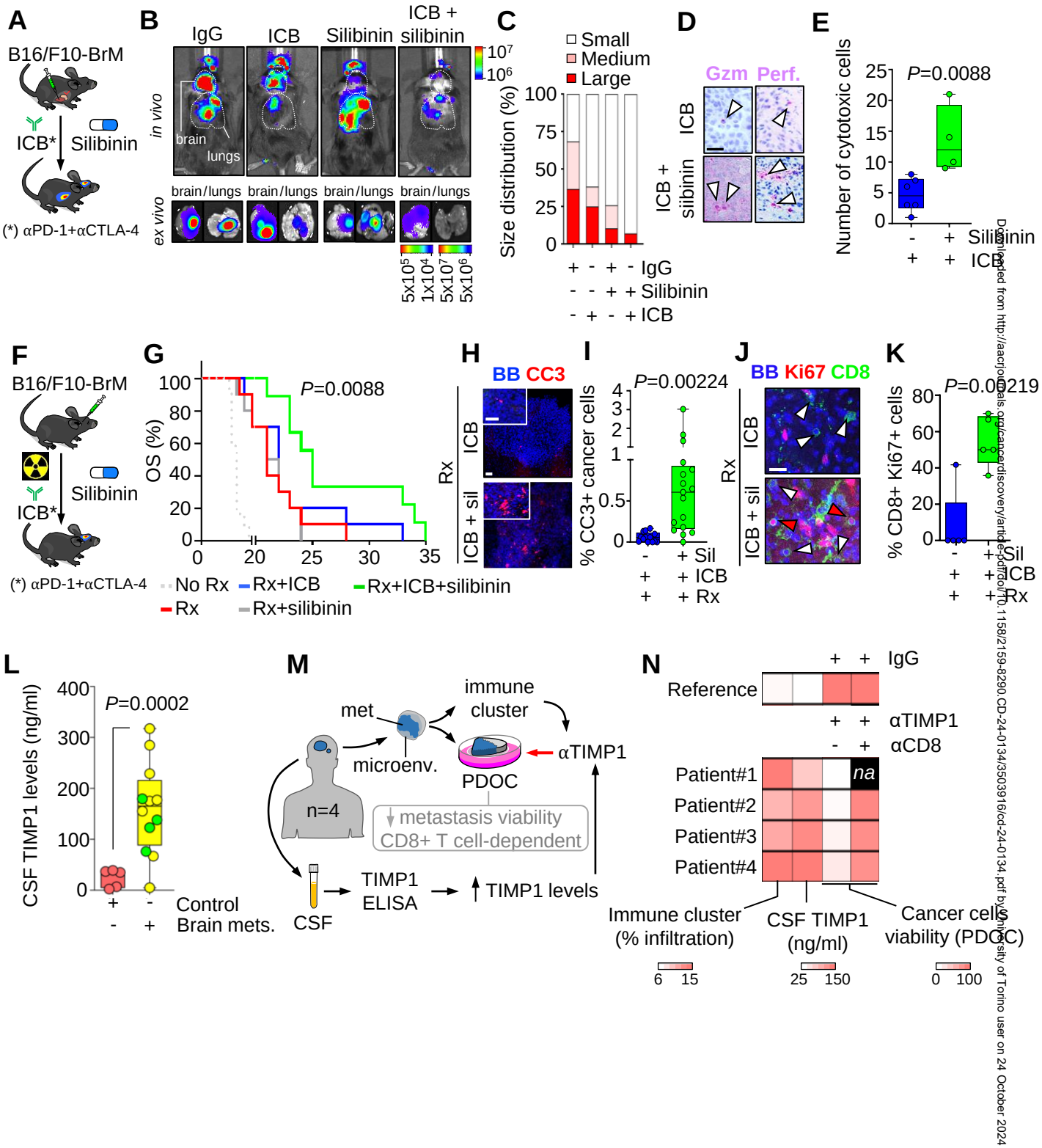

Figure 7